UiO : Department of Geosciences
University of Oslo

An idealized study of flow across submarine canyons

Analytical and numerical approaches to canyon dynamics with applications to the LoVe ocean region

Anna Lina Petrusevičiūtė Sjur

Master's Thesis, Autumn 2021

Abstract

Motivated by the possible connection between the many submarine canyons and the high bioproductivity in the Lofoten-Vesterålen (LoVe) ocean region, this study investigates the flow over an idealized continental slope with a submarine canyon, focusing on cross-slope transport. An important feature is the addition of a well-developed eddy-field, and also the inclusion of periods with reversed wind. In addition, the suitability of quasi-geostrophic theory for predicting flow over a canyon is studied. Both a stratified and a single-layer analytical, quasi-geostrophic model for flow over a slope with topography are developed, based on atmospheric Mountain-wave theory, and numerical model simulations of along-shore wind driven flows are conducted.

Numerical model simulations show that there is an asymmetrical response to flow direction in early flow stages. Under retrograde conditions (flow in the same direction as the topographic wave propagation), there is increased cross-slope transport when a canyon is included, while under prograde conditions (flow in the opposite direction of the topographic wave propagation), the canyon has little effect on the transport. The analytical model predicts this asymmetry to be due to arrested topographic waves resonating with the canyon under retrograde flow. Comparing wavelengths of the arrested topographic waves between the theoretical quasi-geostrophic models and numerical model simulations, we find good agreement, especially in unstratified systems. There is also qualitatively good agreement between flow patterns for prograde flow between the analytical and numerical models.

The slope currents in the LoVe ocean region are highly unstable, motivating us to further explore how increased cross-slope transport, and thus increased nutrient concentration in the shelf region, can occur under these flow conditions. Two possible mechanisms are further explored; 1) the effect of high eddy-activity, both under prograde and retrograde conditions, and 2) periods of reversed wind under mean prograde conditions. We find the same asymmetry under high eddy-activity as for early flow stages, with increased transport in canyon-runs for retrograde flow, and little difference between canyon and no-canyon runs for prograde flow. However, when periods of reversed winds are included in the prograde runs, we see heightened transport in canyon runs in the period after the wind reversal, compared to no-canyon runs. Since observations show periods of winds opposing the flow direction in LoVe, this mechanism may be part of the reason why we see such high bioproductivity in the region.

Acknowledgements

First and foremost, I would like to thank my supervisor, Pål Erik Isachsen, for his engagement, availability and constructive feedback, and for suggesting a thesis project both challenging and rewarding. Without him, writing this thesis would not have been possible.

I am grateful for all the people I have gotten to know during my Master's studies. Thanks for the lunch breaks, puzzling, procrastination, conversations and encouragement. I would also like to thank the God-morgen-møte!-gang, for getting me up in the morning through the seemingly endless rounds of home office. As we say, none mentioned, none forgotten. Without you, I doubt I would have kept my sanity.

A special thank-you goes out to Jan-Adrian, for being there since the day I started my Bachelor studies, to Martin, for making my flip-book dream come true, and to Anna, for the emotional support and culinary experiences.

Thank you, mom, for providing me a safe harbor, and thank you, dad, for always being so proud of me. And to my friends, which always give me the support I need. Because of you, I knew that I could get to where I am today.

Anna Lina Petrusevičiūtė Sjur
June 2021
Oslo

Contents

List of Figures

List of Tables

List of Abbreviations

EKE	eddy kinetic energy
LoVe	Lofoten-Vesterålen
MKE	mean kinetick energy
QGPV	quasi-geostrophic potential vorticity
RMSD	root mean square deviation
ROMS	Regional Ocean Modeling System
SSH	sea surface height
WOD18	World Ocean Dataset 2018

CHAPTER 1

Introduction

1.1 Motivation

The continental shelf off the Lofoten-Vesterålen (LoVe) archipelago in Northern Norway is known as an important site for aquatic life, and for its high marine productivity. In spring and summer, the area is an internationally valuable feeding and spawning area for several fish species, and it is the main spawning area for Northeast Arctic cod and haddock (Quillfeldt, 2010).

Large fish stocks are dependent on plankton growth, which is again limited by the availability of resources, like nutrients and light. Liebig's *Law of the Minimum*, stating that growth is controlled by the scarcest resource, has traditionally been used to explain the limitation of plankton growth. In the ocean, nitrate is usually considered to be the limiting factor, and concentration of said nutrient in the euphotic zone regulates the plankton blooming (Kämpf and Chapman, 2016, pp. 11–18). Nitrate is quickly exhausted, so a consistent supply is needed for the continuation of plankton growth. This could happen through intrusion of nutrient-rich deep ocean water onto the shelf. However, the steep continental slope off LoVe sets up a strong potential vorticity gradient, acting as a barrier between the shelf region and the open ocean. Flowing along this shelf break is the Norwegian Atlantic Slope Current (Fer et al., 2020). In order to have renewal of the coastal water, some dynamics must be present, facilitating the flow in crossing isobaths.

Looking at the map of the LoVe ocean region in Figure 1.1, we see that multiple submarine canyons cut into the continental slope. Bosley et al., 2004 showed that physical processes can lead to concentration of marine organisms in the vicinity of submarine canyons, as the canyon affects the transport of nutrients. Several modeling studies, e.g., Jordi, Klinck, et al., 2008; Jordi, Orfila, et al., 2005; Skliris, Goffart, et al., 2001, show that the presence of a submarine canyon can lead to a large cross-slope water exchange. However, the response depends on the direction of the along-slope flow, which can be either prograde (same direction as the topographic wave propagation), or retrograde (opposite direction of the topographic wave propagation). For retrograde flow, strong on-shore transport occurs, while for prograde flow, the exchange is weaker (Allen and Durrieu de Madron, 2009; Klinck, 1996; She and Klinck, 2000). Spurgin and Allen, 2014 even found that numerical simulations of prograde flow over a canyon exhibits net downward nitrate advection, suggesting a reduction in

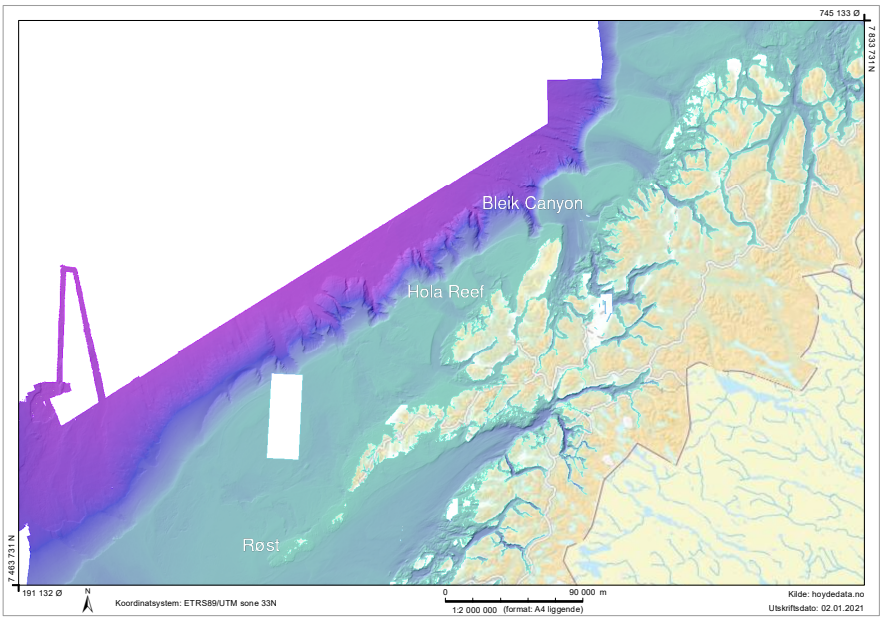

Figure 1.1: Ocean bathymetry off the LoVe archipelago. Purple and light blue signify deeper and shallower regions, respectively. White regions represent missing data. Map is downloaded from dybdedata.no, ©Kartverket.

productivity in nitrate-limited areas.

Studying flow over a submarine canyon, the question arises whether the flow patter can be described theoretically. Some studies suggest that the asymmetrical response to along-shelf flow direction may be related to the canyon's influence on the propagation of Kelvin waves or continental shelf-waves (Allen and Durrieu de Madron, 2009; Killworth, 1978). Using a coastal-trapped wave model, Zhang and Lentz, 2017 showed that the increased transport for retrograde flow over a shelf valley is the result of arrested coastal-trapped waves resonating with the valley, and establishing lee waves downstream of the valley. These lee waves can give large lateral fluctuations and increased transport. Because of the similarity in the physical set-up between shelf valleys and submarine canyons, this is expected to be applicable to submarine canyons as well. Further, Zhang and Lentz, 2018 developed scales for along-valley transport in both prograde and retrograde flow regimes. However, in the study of Zhang and Lentz, the problem of arrested coastal-trapped waves was solved numerically.

A somewhat related problem as flow over a submarine canyon is the atmospheric flow over a mountain. In both situations, we have relatively small perturbations of the lower boundary. Held, 1983 analytically describes the lee wave forming due to arrested planetary waves interacting with a mountain, using quasi-geostrophy. Held considered Rossby waves supported by the planetary β-effect, which are similar to topographic waves supported by a sloping bottom, in that they both result from a tendency towards conservation of potential vorticity. The

likeness between the two physical problems makes it alluring to investigate how well-suited quasi-geostrophy is to describe the flow response over a submarine canyon. To our knowledge, the mountain wave theory developed by Held has not been applied to submarine canyons before.

Returning to LoVe, the high concentration of submarine canyons in the area could be part of the explanation to why there is such high bioproductivity in the area. Since submarine canyons can enhance the cross-shore transport and induce renewal of the coastal water masses, nutrients can be transported onto the shelf. However, the slope current off Northern Norway is flowing in the same direction as the topographic waves, making it a prograde flow. As stated earlier, model studies have shown that there is less exchange present under prograde flow conditions, making the high bioproductivity in LoVe a possible paradox.

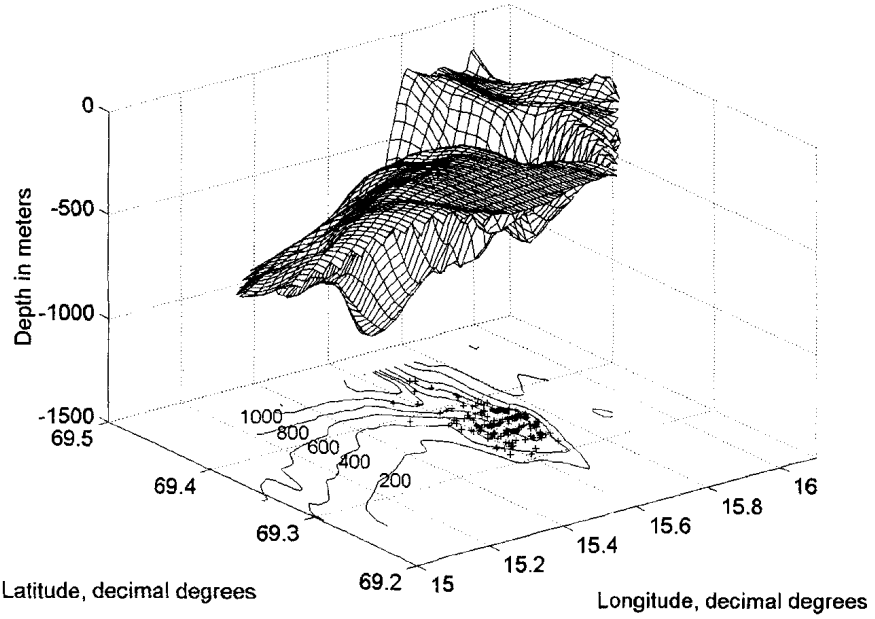

Figure 1.2: Bleik Canyon, situated outside Andøya in Vesterålen, showing 180 documented sightings of sperm whales. Figure from Ciano and Huele, 2001

Yet, previous studies focus on the exchange in early stages of the flow, where the eddy field is not fully developed. In the case of LoVe, observations reveal high eddy kinetic energy (EKE) in the area (Søiland and Rossby, 2013), and eddy-resolving numerical ocean simulations have shown that the flow is the most unstable over the steep Lofoten escarpment (Isachsen, 2015). High eddy activity can in itself increase the cross-slope transport through lateral mixing. But, observations of marine life suggests that the canyons also play an important role in the local ecosystem. As an example, there is a high concentration of sperm shale sightings in the Bleik canyon, as seen in Figure 1.2, indicate that these canyons are especially productive.

A few studies have investigated the effect of a canyon on the eddy field. Saldías

and Allen, 2020, which studied retrograde wind-driven flow along a continental slope, found that the inclusion of a canyon modifies the eddy field, increasing the wavelength of the instabilities downstream of the canyon. Jordi, Klinck, et al., 2008 studied the interaction of prograde flow produced by an unstable density front with a canyon, and found that both frontal instability and a canyon modifies the flow field and enhances the cross-slope exchange. However, in this study, the transport was calculated over a plane limited to the vicinity of the canyon, not taking into account conservation of mass. Common for both of these studies is the short durations of the model runs, with a runtime of 25 and 20 model days, respectively. The effect of a canyon on a well-developed eddy field is thus poorly understood. Since eddies are shown to alter the flow, even in early flow stages, we want to further explore how the cross-slope transport is affected by submarine canyons and flow direction in a highly active eddy field. Since the currents in LoVe are known as highly unstable, the high bioproductivity may be connected to the interaction between submarine canyons and the eddy field.

Another possibility for increased cross-slope transport are episodically winds opposing the prograde flow direction. Model simulations with realistic topography have shown that short wind bursts can induce increased cross-slope transport (Ardhuin et al., 1999; Skliris, Goffart, et al., 2001). Using a high-resolution hydrodynamic model coupled to a coastal plankton ecosystem model, Skliris and Djenidi, 2006 showed that a period of reversal of wind in a prograde system increased the nitrate concentration in the upper ocean layer through vertical turbulent diffusion. Wind reanalysis (ERA5) data from the LoVe area does exhibit periods of winds in the opposite direction of the slope current (see Figure 3b in Fer et al., 2020). We therefore speculate that wind reversal in a well-developed eddy field may also affect the cross-slope exchange, leading to increased onshore transport of nutrients.

1.2 Research questions

Motivated by the high bioproductivity in the LoVe ocean region, this thesis aims to explore how cross-slope exchange can occur in the presence of a submarine canyon under prograde flow regimes. Especially, the role of reversed wind and eddy activity will be studied. For completeness and comparison, the effect of eddy activity on transport in retrograde flow regimes will be studied as well.

Additionally, as we seek to find an analytical model of the flow response to a canyon, an equally important part of this thesis will be to evaluate the applicability of quasi-geostrophic theory to the problem of flow over a submarine canyon. To the author's knowledge, an analytical model describing arrested topographic waves interacting with the topography has not been applied to submarine canyons before.

This raises the following research questions:

- Can quasi-geostrophic theory be used to describe flow patterns over a submarine canyon?
- How does high eddy-activity affect the cross-slope exchange due to a submarine canyon?

- What is the effect of periods of reversed wind on the cross-slope exchange under mean prograde flow over a canyon?

With the purpose of answering these questions, a numerical ocean model is set up, and a series of numerical experiments are carried out. We will have a qualitatively and process-oriented focus, and will thus set up an idealized model. By doing so, we will have full control over the different parameters, and can vary them systematically.

1.3 Outline

The rest of the thesis is organized as follows:

Chapter 2 presents derivations of analytical models for flow over a submarine canyon in a quasi-geostrophic framework. Both a barotropic and a baroclinic model are presented.

Chapter 3 introduces the numerical model set-up used in this study. This section also contains descriptions of the numerical experiments carried out.

Chapter 4 presents results from the numerical experiments, including comparison with analytical theory.

Chapter 5 contains discussion of the result. Also, limitations of the thesis are discussed.

Chapter 6 concludes the thesis, featuring a summary and main contributions. A section on future research is also included.

Appendix A features additional figures.

Appendix B contains derivations of the quasi-geostrophic equations.

CHAPTER 2

Theoretical model

Drawing inspiration from Held, 1983, we will use a quasi-geostrophic framework to analyze flow over a canyon. Held showed how atmospheric flow over topography can excite planetary Rossby waves, given the right flow properties. We will have a similar approach as Held, but consider topographic waves supported by a sloping bottom instead of the planetary β-effect.

Our goal is thus to develop an analytical model explaining the asymmetrical response to along-shore flow over a submarine canyon. In Section 4.2, we will assess the agreement between our analytical model and numerical model runs.

We will start by presenting the quasi-geostrophic potential vorticity (QGPV) equations, before we apply them to barotropic and baroclinic flows along a sloping bottom with white spectered topography. Lastly, we will look into how a submarine canyon affects the theoretical flow response.

2.1 Quasi-geostrophic equations

A systematic derivation of the quasi-geostrophic equations based on scaling theory was first done by Jules Charney in 1948 (Vallis, 2017). As the name suggests, the equations apply to flow in close to geostrophic balance. Here, we will present the QGPV equations, and the assumptions leading to them. For a derivation of the equations, see Appendix B.

The main assumptions are:

- The flow is in near-geostrophic balance, meaning that the Rossby number $Ro = U/Lf$ is small. Here, U and L are respectively a characteristic velocity and length scale, and f is the Coriolis parameter.
- Variations in the Coriolis parameter are small. Specifically, for a β-plane where the Coriolis parameter can be expressed as $f = f_0 + \beta y$, we have $|\beta L|/|f_0| = \mathcal{O}(Ro)$
- The bottom topography h_B is small compared to the total depth h_0, that is, $|h_B|/h_0 = \mathcal{O}(Ro)$.
- Similarly, the surface elevation η is small compared to the total depth; $|\eta|/h_0 = \mathcal{O}(Ro)$.

Further, we have to distinguish between barotropic and baroclinic flow, since the two regimes allow different interior vertical flow structures. In a barotropic flow, surfaces of constant pressure are parallel to surfaces of constant density. Since all density surfaces are parallel to the sea surface, the pressure gradient driving the horizontal flow will not vary with depth, and the flow itself will be two-dimensional in the interior. An exception from this is in the Ekman layers, where we can have a shear in the flow due to friction. In baroclinic flow, surfaces of constant pressure are inclined to surfaces of constant density. The horizontal pressure gradient thus varies with depth, and the flow can have a vertical shear.

The terms barotropic and baroclinic can be a bit ambiguous, since the same system can have both barotropic and baroclinic modes. We therefore define a barotropic model as a 1-layer model, while a baroclinic model refers to a stratified model.

For barotropic flow, the QGPV equation can be written as

$$\frac{D_g}{Dt}\left(\nabla^2\psi + \beta y + \frac{f_0(h_B - \eta)}{h_0}\right) = -r\nabla^2\psi \tag{2.1}$$

where

$$\frac{D_g}{Dt} = \partial_t + u_g\partial_x + v_g\partial_y.$$

Here, ∂_t denotes the partial derivative with respect to t. The partial derivative with respect to other variables are defined similarly. Further, u_g and v_g are the geostrophic velocities. The streamfunction ψ is defined so that

$$u_g = -\partial_y\psi, \qquad v_g = \partial_x\psi, \qquad \zeta_g = \nabla^2\psi.$$

As is conventional, $\zeta_g = \partial_x v_g - \partial_y u_g$ is the relative vorticity. The right side of Equation (2.1) is a forcing term expressing the net effect of a thin bottom friction layer, often called Ekman friction, with r being the Ekman drag coefficient.

For baroclinic flow, the QGPV equation is given as

$$\frac{D_g}{Dt}\left(\nabla^2\psi + \partial_z\left(\frac{f_0^2}{N^2}\partial_z\psi\right) + \beta y\right) = 0, \tag{2.2}$$

with the bottom boundary condition

$$\frac{f_0}{N^2}\frac{D_g}{Dt}\partial_z\psi\bigg|_{z=z_b} = -\mathbf{u}_g\cdot\nabla h_B - r\nabla^2\psi, \tag{2.3}$$

which is a buoyancy equation. Here,

$$N^2 \equiv -\frac{g}{\rho_0}\partial_z\rho_0$$

is the squared Brunt–Väisälä frequency, where g is the gravitational constant and ρ_0 is the background density. This parameter, also known as the buoyancy frequency, is a measure of the stability of the fluid, and can be used as a measure of fluid stratification.

The first term on the left hand-side in Equation (2.3) is the vertical flow resulting from flow over topography, while the second term is the vertical velocity at the top of the bottom Ekman layer, which is proportional to the relative vorticity.

2.2 Barotropic flow along a slope

We will now consider barotropic flow over sloping topography in a quasi-geostrophic framework. First, we will examine the possibility of standing topographic waves, arrested by the mean flow. We will then look at how these waves can be excited by a submarine canyon.

The coordinate system is defined so that the x-axis extending from west to east, and the y-axis from south to north. Later, in the barotropic model, we will include a z-axis, which is increasing with height and equal to zero at the bottom. We assume flow over a slope with constant steepness α, and some topography h_T', so that the seabed height h_B can be expressed as

$$h_B = \alpha x + h_T'(x, y). \tag{2.4}$$

This gives a sloping bottom with increasing depth towards the west, similar to the conditions in LoVe.

Both terms in Equation (2.4) are assumed to be small compared to the mean depth h_0. Here, and later, the prime denotes that the variable is assumed to be small, so αx is assumed to be larger than h_T'. In our case, h_T' describes the canyon topography.

We also assume a stationary mean meridional flow V, which may vary in the x-direction. The full flow can hence be expressed as

$$\mathbf{u} = u'\hat{\mathbf{i}} + (V(x) + v')\,\hat{\mathbf{j}}, \tag{2.5}$$

where u' and v' are perturbations from the mean, assumed to be small compared to V.

Further, we define a streamfunction ψ', so that

$$-\partial_y\psi' = u', \qquad \partial_x\psi' = v', \qquad \nabla^2\psi' = \zeta'. \tag{2.6}$$

Note that ψ' does not describe the horizontal shear in V, only the perturbation flow.

Substituting Equation (2.4) and Equation (2.5) into Equation (2.1), and linearizing, i.e., including only terms containing one prime, we obtain

$$(\partial_t + V\partial_y)\,\nabla^2\psi' - \left(\partial_x^2 V + \frac{f_0}{h_0}\alpha\right)\partial_y\psi' = -V\frac{f_0}{h_0}\partial_y h_T' - r\nabla^2\psi'. \tag{2.7}$$

In the above equation, we have included Ekman friction as a linear damping on the perturbation vorticity, and not the full vorticity of the flow, since we only want to include dynamics of the same scale, i.e., of primed variables. We have also assumed a rigid lid, so that η is ignored. Since the scale of the flow response to the topography is assumed to be small-scaled, we also omit the β-term. The h_T'-term is included on the right-hand side, since it acts as a forcing.

Now, we want to identify an eventual standing wave arrested by the mean flow. By writing the perturbation streamfunction ψ' as a Fourier series

$$\psi' = \mathrm{Re}\left[\sum_{k,l,\omega}\hat{\psi}_{k,l,\omega}e^{ikx+ily-i\omega t}\right],$$

we find that the dispersion relation for unforced waves is

$$\omega = Vl + \frac{\left(\frac{\alpha f_0}{h_0} + \partial_x^2 V\right) l}{\kappa^2},$$

where k and l are the zonal and meridional wavenumber, respectively. The variable ω is the angular frequency. Here, $\kappa^2 = k^2 + l^2$ is the full wavenumber. From the dispersion relation, we can find the meridional phase velocity c_y as

$$c_y = \frac{\omega}{l} = V + \frac{\alpha f_0}{h_0 \kappa^2} + \frac{\partial_x^2 V}{\kappa^2}. \tag{2.8}$$

This is the phase velocity of topographic waves, where we have included the effect of a lateral shear in the meridional velocity.

Ignoring the lateral shear in the mean flow for a moment, we see that the direction of the topographic waves relative to the mean flow is determined by the orientation of the slope and the sign of the Coriolis parameter. In the Northern Hemisphere, topographic waves travel with shallow water to the right, while in the Southern Hemisphere, the waves will travel with shallower water to the left.

It is now straightforward to find the wavenumber of the topographic wave arrested by the mean flow by setting $c_y = 0$ and solving for κ. Doing so, we find that the stationary barotropic topographic wavenumber is given by

$$\kappa^2 = -\left(\frac{\alpha f_0}{h_0 V} + \frac{\partial_x^2 V}{V}\right) \equiv \kappa_{s,bt}^2. \tag{2.9}$$

To see how a canyon can excite the response, we now consider the stationary version of Equation (2.7), assuming that both the streamfunction and the topography can be written in terms of Fourier series on the form

$$\psi' = \mathrm{Re}\left[\sum_{k,l} \hat{\psi}_{k,l} e^{ikx+ily}\right], \qquad h_T' = \mathrm{Re}\left[\sum_{k,l} \hat{h}_{k,l} e^{ikx+ily}\right], \tag{2.10}$$

where $\hat{\psi}_{k,l}$ and $\hat{h}_{k,l}$ are Fourier coefficients. Combining Equation (2.10) and Equation (2.7), this time including the forcing, we find that the streamfunction can be expressed in the wavenumber domain as

$$\hat{\psi}_{k,l} = \hat{h}_{k,l} \frac{f_0}{h_0} \left(\kappa^2 + \frac{f_0 \alpha}{h_0 V} + \frac{\partial_x^2 V}{V} - i\frac{r\kappa^2}{Vl}\right)^{-1}.$$

Or, recognizing the expression for the stationary topographic wavenumber defined in Equation (2.9),

$$\hat{\psi}_{k,l} = \hat{h}_{k,l} \frac{f_0}{h_0} \left(\kappa^2 - \kappa_{s,bt}^2 - i\frac{r\kappa^2}{Vl}\right)^{-1}. \tag{2.11}$$

Ignoring the friction term for a moment, we see that we have a singularity at $\kappa^2 = \kappa_{s,bt}^2$, describing resonance between the arrested wave and the topography. The addition of friction removes the singularity, dampening the response, and also introduces a phase shift. For resonance to occur, V must be in the opposite direction of the relative phase velocity of the topographic waves, i.e., the flow must be retrograde.

2.3 Baroclinic flow along a slope

In the baroclinic case, we assume the same bathymetry as in Equation (2.4). Again, we assume a stationary mean meridional flow V, but this time dependent both on x and z, since baroclinic flow inherently allows a vertical shear.

In order to arrive at simple, analytical expressions, we assume that the flow V is separable with a linear dependency on height, so that it can be written as

$$V(x, z) = V_0(x) \cdot P(z),$$

where

$$P(z) = az + b, \qquad a,\, b \in \mathbb{R}.$$

The full velocity field is then

$$\mathbf{u} = u'\hat{\mathbf{i}} + (V_0(x)\,(az + b) + v')\,\hat{\mathbf{j}}. \tag{2.12}$$

We note that the velocity at the bottom, V_b, and the vertical shear in the flow, $\partial_z V$, can be written as

$$V_b = V_0 b, \qquad \partial_z V = V_0 a,$$

where we have assumed that $z = 0$ at the bottom. For simplicity, we also assume that the buoyancy frequency N is constant.

Now, to find the dispersion relation in the baroclinic case, we assume a stationary solution, and thus drop the time derivative in the interior QGPV-equation. By doing this, we get an analytically solvable differential equation, at the expense of a general expression for the dispersion relation. Nevertheless, we are still able to find the wavenumber of the stationary waves.

Substituting Equation (2.12) into the stationary version of the baroclinic QGPV equation (Equation (2.2)) and linearizing, we are left with

$$V_0 \partial_y \left(\nabla^2 \psi' + \frac{f_0^2}{N^2} \partial_z^2 \psi \right) - \partial_y \psi' \partial_x^2 V_0 = 0.$$

We now assume that the streamfunction can be written as a Fourier series on the form

$$\psi' = \mathrm{Re}\left[\sum_{k,l,\omega} \hat{\psi}_{k,l,\omega}(z) e^{ikx + ily - i\omega t} \right], \tag{2.13}$$

where the Fourier coefficients $\hat{\psi}_{k,l,\omega}(z)$ are dependent on the height z.

This yields the second order differential equation

$$\partial_z^2 \hat{\psi} = \left(\frac{N^2}{f_0^2} \kappa^2 + \frac{N^2}{f_0^2 V_0} \partial_x^2 V_0 \right) \hat{\psi}. \tag{2.14}$$

Depending on the sign of the expression in the parentheses, we can have either a wave solution or an exponential solution in the vertical.

Assuming a positive expression in the parentheses, the solution is given by

$$\hat{\psi}(z) = \psi_0 e^{-\mu z}, \qquad \mu = \frac{N}{|f_0|}\left(\kappa^2 + \frac{\partial_x^2 V_0}{V_0}\right)^{\frac{1}{2}} \tag{2.15}$$

Here, ψ_0 is some constant. For simplicity, the subscript of $\hat{\psi}(z)$ is left out. We have only kept the solution decaying with height, as the wave is assumed to be trapped to the bottom, with a negligible amplitude at the surface. This assumption is a potential shortcoming of our model, as it assumes that $1/\mu$ is much smaller than h_0. Note that in the case where V does not vary in the horizontal direction, Equation (2.15) is the general solution, and not just the solution to the steady problem with exponential variation in the interior.

In the case where the expression in the parentheses is negative, the solution to Equation (2.14) is given by

$$\hat{\psi}(z) = \psi_0 e^{imz}, \qquad m = \pm\frac{N}{|f_0|}\left(-\kappa^2 - \frac{\partial_x^2 V_0}{V_0}\right)^{\frac{1}{2}} \tag{2.16}$$

Now we apply the bottom boundary condition. We substitute the expression for the bottom height (Equation (2.4)) and the flow field (Equation (2.12)) into the bottom boundary condition (Equation (2.3)). Linearizing and writing the perturbed velocities in terms of the streamfunction, we get

$$(\partial_t + bV_0\partial_y)\,\partial_z\psi' - \partial_y\psi'\partial_z V_0 - \frac{\alpha N^2}{f_0}\partial_y\psi' = -\frac{VN^2}{f_0}\partial_y h_T' - \frac{rN^2}{f_0}\nabla^2\psi'. \tag{2.17}$$

As for the barotropic case, we now consider the steady, forced version of Equation (2.17). Writing h_T' as a Fourier series as described in Equation (2.10), and ψ' as described by Equation (2.13), using either Equation (2.15) or Equation (2.16) for the vertical structure, we find an expression for the constant ψ_0.

When we have a wave structure in the interior, the solution is

$$\psi_0 = \hat{h}N\left(\frac{f_0\partial_z V}{NV_b} + \frac{\alpha N}{V_b} + i\left(-\kappa^2 - \frac{\partial_x^2 V}{V_0}\right)^{\frac{1}{2}} - i\frac{rN\kappa^2}{V_b l}\right)^{-1},$$

while when the vertical structure is exponential, the solution is

$$\psi_0 = \hat{h}N\left(\left(\kappa^2 + \frac{\partial_x^2 V}{V_0}\right)^{\frac{1}{2}} + \frac{f_0\partial_z V}{NV_b} + \frac{\alpha N}{V_b} - i\frac{rN\kappa^2}{V_b l}\right)^{-1}. \tag{2.18}$$

Looking at the two above solutions, we see that, when ignoring friction, a singularity dependent on κ is only possible in Equation (2.18). Since we want to explore the possibility of arrested waves resonating with the topography, we will assume a solution for the interior structure as described by Equation (2.18), and thus discard the other solutions.

Again, we want to find the dispersion relation for the unforced wave, setting the right side of Equation (2.17) equal to 0. Writing the streamfunction as a

Fourier series as described in Equation (2.13) and Equation (2.18), we find that the angular frequency ω can be written as

$$\omega = V_b l + \frac{\alpha N^2 l}{f_0 \mu} + \frac{\partial_z V l}{\mu},$$

with μ as described in Equation (2.15). This is the stationary dispersion relation when there is a x-dependency in the mean flow, and the general dispersion relation in the absence of such a shear.

Thus, the meridional phase velocity is given as

$$c_y = \frac{\omega}{l} = V_b + \frac{\alpha N^2}{f_0 \mu} + \frac{\partial_z V}{\mu} = 0 \tag{2.19}$$

or in the case where $\partial_x^2 V_0 / V_0 = 0$, the phase velocity is

$$c_y = V_b + \frac{|f_0| \alpha N}{f_0 \kappa} + \frac{|f_0| \partial_z V}{N \kappa}. \tag{2.20}$$

Ignoring the shear in the mean flow, we see that the direction of the topographic wave relative to the bottom flow depends on the slope orientation and the Coriolis parameter. Just as in the barotropic case, the waves travel with shallow water to its right in the Northern Hemisphere, and to its left in the Southern Hemisphere.

The last term in Equation (2.20) is not related to the topography, but to the vertical shear in the flow. This term is the phase velocity of an Eady wave, i.e., waves associated with a horizontal density gradient.

Solving for the wavenumber κ in Equation Equation (2.19), we find that the wavenumber of the arrested wave in a baroclinic system can be expressed as

$$\kappa^2 = \left(-\frac{f_0 \partial_z V}{N V_b} - \frac{\alpha N}{V_b} \right)^2 - \frac{\partial_x^2 V}{V_0} \equiv \kappa_{s,bc}^2. \tag{2.21}$$

The full solution is thus

$$\hat{\psi}(z) = \hat{h} N \left(\left(\kappa^2 + \frac{\partial_x^2 V}{V_0} \right)^{\frac{1}{2}} + \frac{f_0 \partial_z V}{N V_b} + \frac{\alpha N}{V_b} - i \frac{r N \kappa^2}{V_b l} \right)^{-1} e^{-\mu z},$$

$$\mu = \frac{N}{|f_0|} \left(\kappa^2 + \frac{\partial_x^2 V_0}{V_0} \right)^{\frac{1}{2}} \tag{2.22}$$

In the absence of a horizontal shear, Equation (2.22) can be reduced to

$$\hat{\psi}(z) = \hat{h} N \left(\kappa - \kappa_{s,bc} - i \frac{r N \kappa^2}{V_b l} \right)^{-1} e^{-\left| \frac{N \kappa}{f_0} \right| z}.$$

Similarly as for the barotropic case, there is a resonance singularity at $\kappa = \kappa_{s,bc}$, which is removed by the inclusion of friction. Again, the bottom flow must be retrograde for resonance to occur.

2.4 White spectrum response

To better understand the flow response to topography, the amplitude and phase spectra of the barotropic and baroclinic streamfunction resulting from a topography containing all wavenumbers, i.e., a white spectrum, is shown in Figure 2.1. This figure shows a similar response as Figure 3.16 in Held, 1983. To the left in Figure 2.1 is the barotropic response, while the baroclinic response is shown to the right.

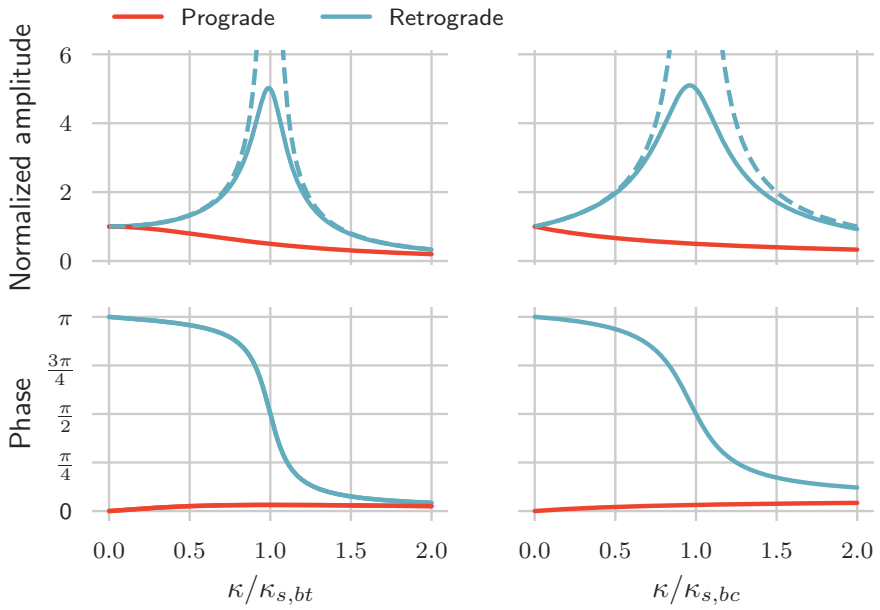

Figure 2.1: Amplitude and phase spectrum of the streamfunction response to a slope with topography containing a uniform distribution of all wavenumbers. Left is barotropic response, right is baroclinic response. Solid lines are for flow with bottom friction and dashed lines are for friction-less flow. Top panels show the amplitude normalized with the maximum amplitude for a prograde flow. Bottom panels show the phase. In all panels, the wavenumber is normalized with the wavenumber of the stationary topographic wave in the retrograde case.

Looking at the amplitude of both the barotropic and baroclinic prograde response to a white spectrum, we see that smaller wavenumbers, i.e. larger wavelengths, are weighted more than larger wavenumbers in the Fourier representation of the streamfunction. Additionally, the response is almost in phase with the topography. This way, the flow functions as a longpass filter of the topography, transmitting longer wavelengths. As a result, the streamfunction of prograde flow over topography resembles a smoothened version of the bathymetry.

We should also note that in Figure 2.1, the wavenumbers on the x-axis are scaled with the wavenumber of the corresponding arrested wave. In the prograde case, this is calculated as $|\kappa^2_{s,bt}|^{\frac{1}{2}}$ and $|\kappa^2_{s,bc}|^{\frac{1}{2}}$, to have real solutions. If $|\kappa^2_{s,bt}|^{\frac{1}{2}}$

and $|\kappa^2_{s,bc}|^{\frac{1}{2}}$ decreases, we see from Figure 2.1 that larger wavenumbers in the topography are expected to be weighted even less in the streamfunction response, resulting in an even smoother flow. Correspondingly, if these variables were to increase, larger wavenumbers are weighted more, allowing the flow to follow the topography to a greater degree. So, according to quasi-geostrophy, the variables predicting the flow response to a given topography are the variables found in the expressions for $\kappa^2_{s,bt}$ and $\kappa^2_{s,bc}$, as declared in Equation (2.9) and Equation (2.21). An important example is that increased flow speed would result in lower values for $|\kappa^2_{s,bt}|^{\frac{1}{2}}$ and $|\kappa^2_{s,bc}|^{\frac{1}{2}}$, resulting in a smoother flow.

Moving on to the retrograde flow, we see from the amplitude spectrum in Figure 2.1 that in the absence of friction, there is a singularity at $\kappa = \kappa_{bt,s}$ and $\kappa = \kappa_{bc,s}$. This signifies that there is resonance between the arrested topographic wave and the topography. We also see that wavenumbers close to the wavenumber of the arrested wave are heavily weighted.

As mentioned, the singularity is removed by including bottom friction. Still, the wavenumber of the topographic wave, and the wave numbers close to it, is heavily weighted in the Fourier representation of the streamfunction response, meaning that the arrested wave will grow in amplitude. Another effect of friction is a phase shift, which depends on κ. From the phase spectrum, we see that the resonant streamfunction is 90° out of phase with the topography.

As for the difference between the response in a barotropic and a baroclinic system, there is a wider band of wavenumbers that are heavily weighted in the baroclinic case, as seen in Figure 2.1. This tells us that there is a wider range of topographies that can give a strong response under baroclinic conditions, given the same wavenumber of the arrested wave in barotropic and baroclinic flow.

2.5 Response to a canyon

We will now consider the flow over a canyon with a Gaussian shape, specifically.

Figure 2.2 shows the barotropic streamfunction response to a Gaussian canyon, given $h_0 = 500\,\mathrm{m}$, $f_0 = 10^{-4}\,\mathrm{s}^{-1}$, $\alpha = 0.025$, $|V| = 0.20\,\mathrm{m/s}$ and $r = 10^{-4}\,\mathrm{s}^{-1}$. The canyon shape h'_T is given by

$$h'_T = -h_0 e^{-x^2/L^2},$$

where h_0 =100 m and L =10×10^3 m. A qualitatively equivalent behavior is seen in a baroclinic system (not shown).

Indeed, as discussed, we see that the prograde barotropic flow resembles a slightly smoothed version of the topography. In the retrograde case, the streamfunction grows in amplitude over a canyon, and exhibits a gradually dampened wave response downstream of the canyon. The degree of dampening is controlled by the friction, and in the case of no friction, the wave signal extends over the whole domain (not shown). An important point is that the strength of the response is dependent on the geometry of the canyon. As we can see from the expressions for the Fourier coefficients of the barotropic and baroclinic streamfunction response (Equation (2.11) and Equation (2.18)), the amplitude of the streamfunction response is the product of the amplitude spectrum of the

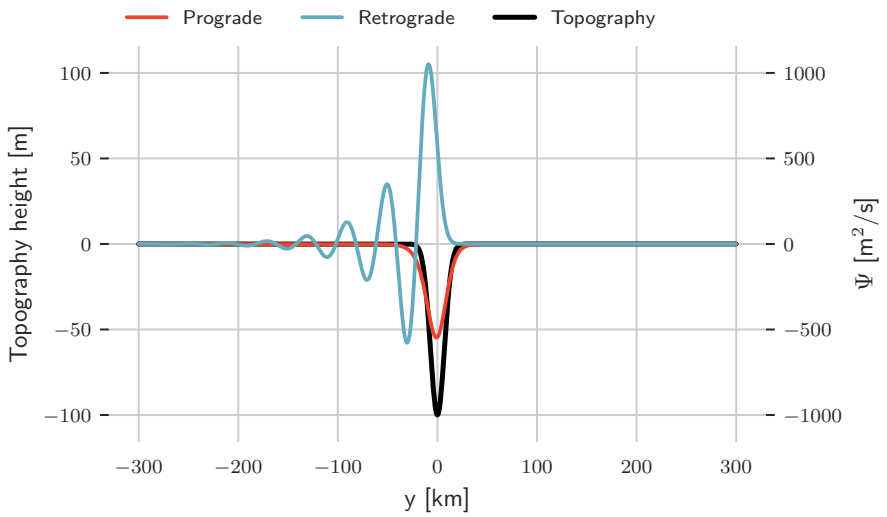

Figure 2.2: Streamfunction response to a slope with a Gaussian canyon as a function of along-slope position in a barotropic system. Prograde flow is towards the right, while retrograde flow is towards the left.

canyon and the amplitude spectrum shown in Figure 2.1. This means that for a prescribed flow, there exists an optimal canyon which maximizes the amplitude of the streamfunction response.

From the definition of the streamfunction (Equation (2.6)), we have that streamlines coincide with the streamfunction contours, and we can thus say something about the horizontal flow response, based on the streamfunction response. In the case of a submarine canyon, we would expect the prograde flow to almost follow isobaths, resembling a wider canyon, given that the flow is suitably slow. As the velocity increases, given that other flow characteristics are unchanged, we would expect the flow to follow the isobaths to a lesser degree, as shorter wavelengths in the topography are weighted less. Similarly, we would expect the flow to follow the isobaths to a greater degree in wider canyons than in narrower canyons, given the same flow characteristics.

For the retrograde response, we would expect a similar horizontal wave pattern downstream of the canyon, as we see for the retrograde streamfunction in Figure 2.1.

CHAPTER 3

Numerical model set-up

In order to see how well our quasi-geostrophic models preform in predicting the flow over a canyon, and to assess the cross-slope transport under varying conditions, we run a series of numerical simulations, which are preformed using the Regional Ocean Modeling System. Here, we will go through the specific set-up of our model, and describe the experiments we conduct.

3.1 The Regional Ocean Modeling System

The Regional Ocean Modeling System (ROMS) is an open source software developed by Rutgers University and the University of California, Los Angeles ocean modeling groups. It is a free-surface, hydrostatic, primitive equation ocean model that uses stretched, terrain-following coordinates in the vertical and orthogonal curvilinear coordinates in the horizontal[1]. The horizontal grid is an Arakawa-C grid, where quantities are evaluated at different positions in the grid. ROMS has been applied in numerous studies, including studies considering submarine canyons (e.g. Saldías and Allen, 2020; She and Klinck, 2000). Since it was initially developed, several versions of ROMS have been launched. In this study, version 3.9 is used.

A thorough description of the ROMS algorithms can be found in Moore et al., 2004; Shchepetkin and McWilliams, 2005; Shchepetkin and McWilliams, 2003. Here, we will go through the specific set-up for our applications.

3.2 Model domain

In our set-up, we use an idealized domain representing a submarine canyon cut into a continental slope. By stripping away unnecessary aspects of the topography, we can more easily identify the effect of the canyon itself. An idealized domain also makes the implementation easier, since we can use Cartesian coordinates in the horizontal and an analytical function for the bathymetry. We will below go through relevant aspects of the domain set-up, which is designed after the domain used by Saldías and Allen, 2020. We first present the bathymetry, before we go through implementation choices.

[1] On the topic "What is ROMS?" from the ROMS forum https://www.myROMS.org/forum/viewtopic.php?t=83

Bathymetry

In this study, the shelf and canyon topography is similar to that used in previous studies on canyon dynamics (Klinck, 1996; Saldías and Allen, 2020). The basin depth $H(x, y)$ is defined by

$$H(x,y) = H_m - \frac{H_s}{2}\left[1 - \tanh\frac{x_m - x - x_0(y)}{a}\right], \tag{3.1}$$

where x and y are the cross-shore position and along-shore position, respectively. The parameter $x_0(y)$ gives the cross-shore distance from the coastal wall to the shelf break, and is given by

$$x_0(y) = x_n + x_b\left[1 - \exp\frac{-|y - y_0|^2}{2b^2}\right]. \tag{3.2}$$

The above equation is where the canyon shape is defined. To construct a continental slope without a canyon, x_0 is set equal to $x_n + x_b$. A description of the different parameters in Equation (3.1) and Equation (3.2), together with the specified value used in model runs, can be found in Table 3.1.

Table 3.1: Parameters for the model bathymetry. *The parameter a is different for some experiments, see Table 3.3 and Table 3.4.

Parameter	Description	Value	Unit
H_m	maximum domain depth	500	m
H_s	depth change from shelf to open ocean	400	m
x_n	offshore canyon distance	12	km
x_b	distance added to x_n to reach shelf break	10	km
x_m	cross-shore domain-length	155	km
y_m	alongshore domain-length	600	km
y_0	alongshore canyon position	300	km
a	slope transition scale	5*	km
b	canyon width-scale	2.5	km

In order to trigger the onset of instabilities in the stratified model runs, random noise is added to the topography. This noise has a normal distribution with zero mean, and a standard deviation of 0.1 m. Without the noise added to the seabed, we found that instabilities took a long time to evolve.

The above configurations give a bathymetry as seen in Figure 3.1. Here, and in the following results, the axes are shifted so that the canyon is centered around y=0, and with x=0 at the coastal wall. Parameters as given in Table 3.1 produces a canyon about 20 km long and 10 km wide at the mouth. The continental shelf is 100 m deep, while the open ocean reaches down to a depth of 500 m.

This idealized canyon is of about the same scale as the canyons situated outside LoVe, in terms of length and width. However, the deep ocean and shelf are deeper in the LoVe ocean region than in our model, with depths of 75-150 m on

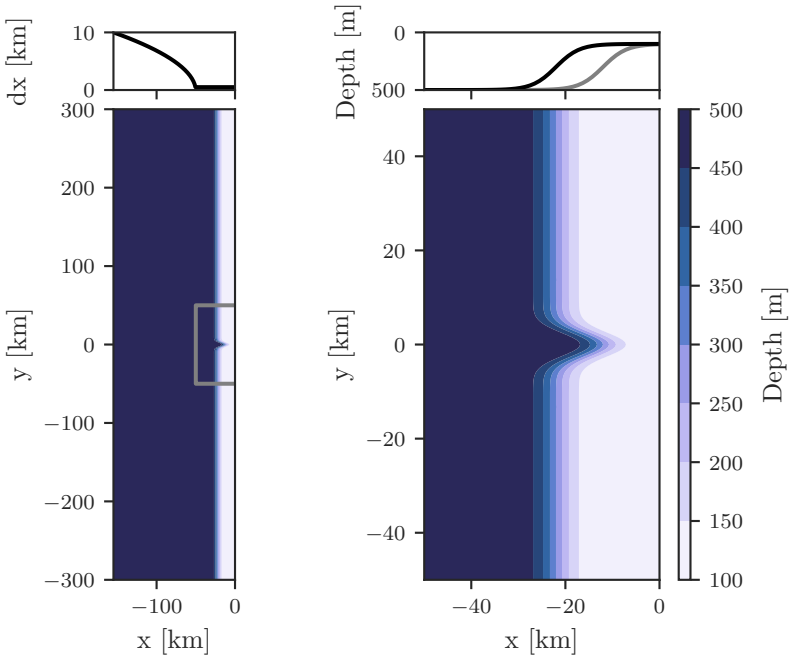

Figure 3.1: Model bathymetry. The two lower panels show the depth as a function of cross-shore (x) and along-shore (y) position. The right panel is a zoomed in version of the area enclosed in a gray box in the left panel. The upper right panel is a side-view of the shelf, with the continental slope in black and the canyon in gray. Top left panel shows the cross-shore grid spacing.

the shelf and 2000-3000 m off the shelf[2]. A deeper model is possible, but would be more resource-intensive, and wouldn't necessarily give a better conceptual understanding.

Boundaries

The model domain is a rectangular basin with a coastal wall at the eastern boundary. Periodic boundary conditions are applied at the northern and southern boundaries, so that the domain represents a channel. At the offshore boundary, a radiation boundary condition is used, while at the continental wall the boundary is closed, with free slip along the wall.

Since the model domain is periodic in the meridional direction, signals originating from the canyon and moving downstream can eventually wrap around and reach the canyon from the upstream direction. This will most likely influence the response. One way to handle this is to consider only the initial response, before waves have time to wrap all the way around. Alternatively, one can be attentive to the effect of waves wrapping around the domain, but nevertheless let the model run for longer. Looking at the map of the LoVe ocean basin in Figure 1.1, we see that multiple canyons cut across the continental slope. Linking our

[2]Values from dybdedata.no.

experiment to the LoVe basin, we can look at the response wrapping around the domain as having multiple succeeding canyons carved into the continental slope.

Horizontal grid spacing

Grid spacing in the along-shore direction is 500 m for the whole domain. In the cross-shore direction, the grid spacing is 500 m within 50 km of the shore, and then gradually increasing towards 10 km at the offshore boundary. For each step towards the offshore boundary after the first 50 km, the cross-shore grid-size is increased with 500 m. This is done to increase computational efficiency. The resulting cross-shore grid spacing is plotted in the top-left panel in Figure 3.1. In total, the length of the domain is 155 km and 600 km in the cross-shore and along-shore direction, respectively.

Vertical layers

In the vertical, we have terrain-following coordinates (also known as σ coordinates and s coordinates), so that -1 and 0 is always at the bottom and surface, respectively. In total, our set-up includes 30 layers, distributed so that the distance between layers are smaller near the surface and bottom. The bottom panel of Figure 3.2 shows a vertical section of the distribution of the layers.

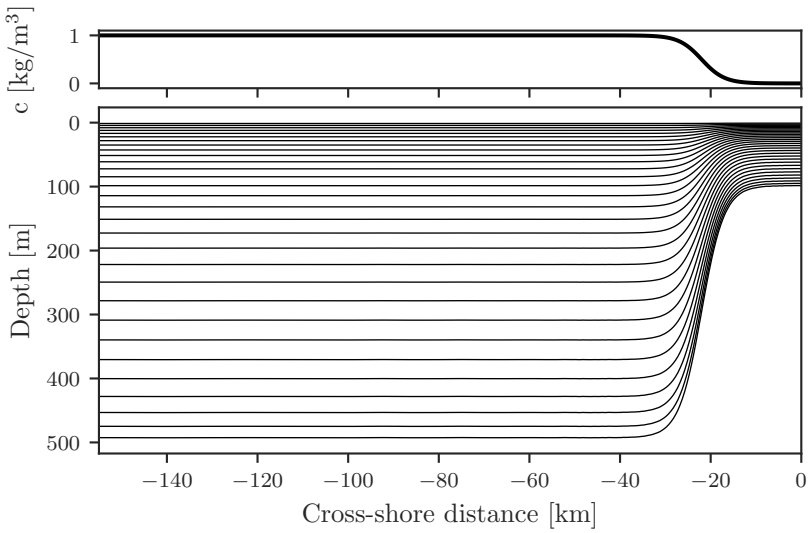

Figure 3.2: Depth of the model's terrain-following s-levels from west to east, together with tracer concentration. Lower panel shows the depths of the horizontal s-levels, which divides the model into a total of 30 layers. Top panel shows the initial tracer concentration c.

Terrain-following coordinates are beneficial for regional applications, since the topography and lower boundary layers are well resolved. However, the use of such coordinates can introduce errors in the pressure-gradient and spurious

diapycnal diffusion (Marchesiello et al., 2009). This can especially be a problem at the canyon rim, where the topography is steep. It is therefore important to monitor the evolution of the properties of the water masses, and experiment with advection schemes and vertical transformation parameters. We found that the 4th-order Akima advection algorithm for temperature, and the 3th-order HSIMT-TVD advection algorithm for salt and tracer gave best results.

3.3 Initializing

When setting up a ROMS application, the initial state of the system must be specified. Here, we will first go through the initial state of the active tracers, which are the temperature and salinity fields. Then we will look at passive tracers. Other variables, as initial velocities and the sea surface height, are set to zero.

Temperature and salinity fields

An active tracer is a tracer that influences the current itself through altering properties included in the equation of motion. Salinity and temperature does this through their effect on water density.

Depending on the experiment, primarily two different active tracer initial states are used. For some experiments used to validate the theoretical model, the initial profiles differ from these two states. We will return to these cases in Section 3.5. The first state is for a system with no stratification. To achieve this, we omit the salinity and only include temperature and set it equal to a constant value through the whole domain. That way, the whole water column has the same density.

The second state is for a stratified system. Here, both temperature and salinity are included. Both are set to be initially only dependent on depth. To construct profiles of temperature and salinity, in-situ measurements from the LoVe basin of these variables are fetched from the World Ocean Dataset 2018 (WOD18). Plots of number of observations per level and cast distribution can be found in Appendix A (Figure A.1 and Figure A.2). Then, the regional mean for each depth level is computed. The resulting profiles can be seen in Figure 3.3. In addition to salinity and temperature, Figure 3.3 also shows the corresponding potential density anomaly and squared Brunt–Väisälä frequency.

While profiles constructed from in-situ measurements are to a degree representative of the actual conditions, these profiles are still a considerable simplification. The profiles are constructed as a mean over time, ignoring that conditions change according to the seasons and even through the day as the incoming solar radiation changes. In reality, we would also expect variations in the horizontal dimensions, with fresher water at the surface closer to the shore, due to freshwater runoffs. However, for our idealized study, these are deemed reasonable simplifications.

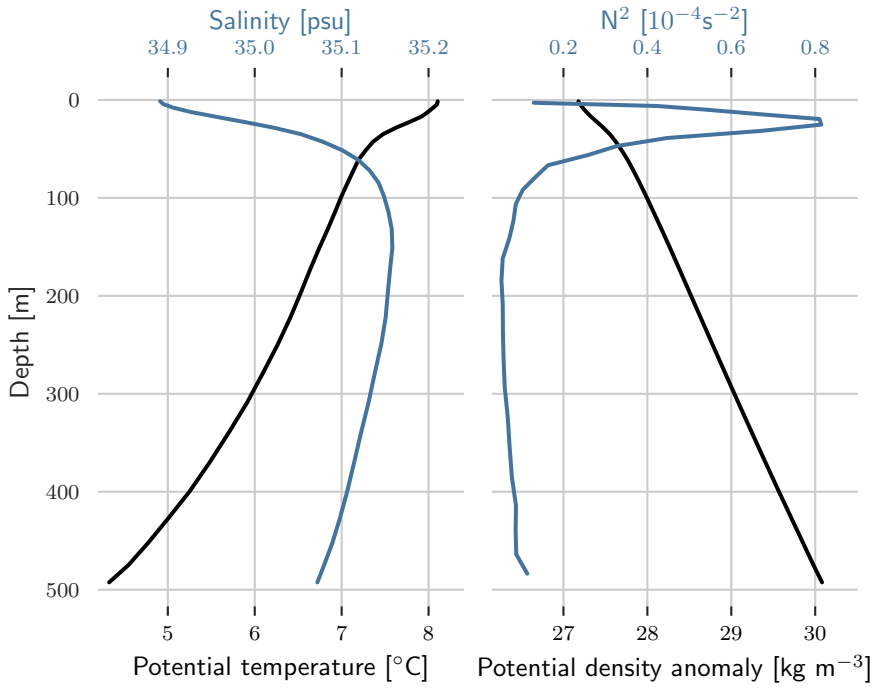

Figure 3.3: Profiles of initial potential temperature, salinity, potential density anomaly and the squared Brunt–Väisälä frequency in the ROMS applications with stratification.

Passive tracer

Passive tracers are variables that don't affect the flow. They can be thought of as dye added to the water, advected by currents and diffused by turbulent stirring.

We want to include a passive tracer acting as a signature for deep ocean water, so that we can estimate the cross-slope exchange by computing the tracer flux. To do so, we set up a passive tracer which initially follows the shape of the bathymetry, with the canyon omitted. At the shore, the concentration is set to zero, while at the open ocean the concentration is 1. The initial tracer concentration $c(x)$ is expressed as

$$c(x) = 1 - 0.5 \left[1 - \tanh \frac{x_m - x_n - x_b - x}{a} \right], \tag{3.3}$$

with parameters as described in Table 3.1. The expression is plotted in the top panel of Figure 3.2.

3.4 Forcing

Along-shore flow is set up by a horizontally uniform meridional surface wind stress. Initially, the model is left unforced for the first 10 days. This is done to

check for spurious vertical velocities. After the initial 10 days, the forcing is linearly increased over 5 days to its maximum magnitude. After day 15, the forcing is held constant. In this set-up, a positive stress represents northward wind, resulting in a prograde flow, while a negative stress gives a retrograde flow.

In some prograde experiments, the forcing is reversed for a period of time. The mean flow over time is then prograde, while (parts of) the flow field becomes episodically reversed. This is called an event, and consists of a sinusoidal wave cycle. To illustrate how the forcing evolves over time, forcing setting up prograde flow, with a wind event between day 50 and 60, is plotted in Figure 3.4. Note that even though the wind event lasts for 10 days, the stress is only reversed for 5 of those days. The length of the wind reversal is based on data exploration of observations of wind direction from Røst airport, south-west in Lofoten. The data is fetched from the Norwegian Centre for Climate Services, seklima.met.no.

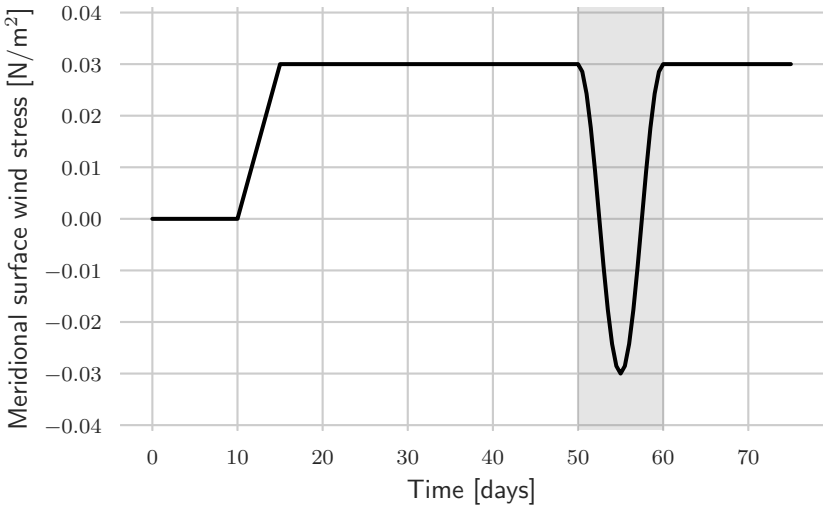

Figure 3.4: Meridional surface wind stress as a function of time, illustrative of the forcing used in model runs. The forcing is zero for the first 10 days, and then linearly increasing over 5 day to its maximum magnitude. After day 15, the forcing is kept constant, except if a wind event is included. An example of a wind event is here shaded in gray between day 50 and 60. In the experiments, the wind event does not necessarily take place in this period. The wind in this plot is from the south. Wind from the north is identical, except for opposite sign.

3.5 Experiments

The numerical experiments carried out can be divided into three categories; a collection of baseline experiments highlighting the asymmetrical response to flow direction; model runs intended for affirmation of the theoretical models described in Chapter 2; and experiments intended for investigating the effect of

eddy activity and reversal of winds. We will go through the main aspects of each category here.

Baseline experiments

In total, eight baseline experiments are carried out. They are constructed from the two choices of initial stratification and flow direction. In addition, experiments both with and without a canyon are included for each choice. An overview of the baseline experiments are given in Table 3.2.

Table 3.2: Characteristics of baseline numerical experiments.

Experiment	**Stratification**	**Flow direction**	**Canyon**
NS-R-NC	No	Retrograde	No
NS-R-C	No	Retrograde	Yes
NS-P-NC	No	Prograde	No
NS-P-C	No	Prograde	Yes
S-R-NC	Yes	Retrograde	No
S-R-C	Yes	Retrograde	Yes
S-P-NC	Yes	Prograde	No
S-P-C	Yes	Prograde	Yes

Validation of theoretical model

For validating the quasi-geostrophic theory described in Chapter 2, we run a series of experiments where we vary parameters effecting the arguments in Equation (2.9) and Equation (2.21). In these experiments, we will only look at retrograde flow, which is where we expect arrested waves. We can then compare theoretical wavelengths with the wavelengths of the arrested waves in model runs.

To validate the model, experiments both with and without stratification are conducted. Unstratified experiments used to validate the barotropic theoretical model are listed in Table 3.3, while stratified experiments used to validate the baroclinic theoretical model are listed in Table 3.4. In the two last experiments listed in Table 3.4, the initial temperature profile differs from that in Figure 3.3. In order to vary the buoyancy frequency N, the temperature profile is here initialized as a linear function, with different slope in the two experiments. The resulting mean N over the slope can be read from Table 3.4.

Additionally, we want to qualitatively evaluate how well the theoretical models describe prograde flow. This is done based on the baseline experiments described in Table 3.2. QG-theory predicts that flow characteristics, specifically V and $\partial_x^2 V$ for barotropic flow and V_b, $\partial_x^2 V$ and $\partial_z V$ for baroclinic flow, affects the streamfunction response, so by inspecting the flow field at different times as the flow evolves, we can assess whether the evolution is in accordance with theory.

Table 3.3: Characteristics of numerical experiments used for validating the barotropic theoretical model. RDRG2 is the non-dimensional quadratic bottom drag coefficient used by ROMS. The parameter a is the slope transition scale, determining the shelf slope, used in the analytical expression for the bathymetry (Equation (3.1)), with units km. The forcing has units Nm^{-2}, and is a surface wind stress.

Label	**Forcing**	**RDRG2**	a
baseline	-0.03	3.0×10^{-3}	5
2×forcing	-0.06	3.0×10^{-3}	5
3×forcing	-0.09	3.0×10^{-3}	5
4×forcing	-0.12	3.0×10^{-3}	5
2×friction	-0.03	6.0×10^{-3}	5
$0.5\times\alpha$	-0.03	3.0×10^{-3}	10

Table 3.4: Characteristics of numerical experiments used for validating the baroclinic theoretical model. RDRG2 is the non-dimensional quadratic bottom drag coefficient used by ROMS. The forcing has units Nm^{-2}, and is a surface wind stress. N is the mean value of the buoyancy frequency over the slope at the beginning of the model run, with units $10^{-2}\mathrm{s}^{-1}$.The parameter a is the slope transition scale used in the analytical expression for the bathymetry (Equation (3.1)), with units km. The last column tells us at which model day the arrested wavelength is evaluated.

Label	**Forcing**	**N**	**RDRG2**	a	**Evaluated**
baseline	-0.03	0.43	3.0×10^{-3}	5	50
2×forcing	-0.06	0.43	3.0×10^{-3}	5	29
3×forcing	-0.09	0.43	3.0×10^{-3}	5	50
4×forcing	-0.12	0.43	3.0×10^{-3}	5	30
2×friction	-0.03	0.43	6.0×10^{-3}	5	40
$0.5\times\alpha$	-0.03	0.43	3.0×10^{-3}	10	50
sN	-0.03	0.30	3.0×10^{-3}	5	41
lN	-0.03	0.62	3.0×10^{-3}	5	31

Eddy activity and periodical reversal of winds

With the intent to investigate eddy activity and periodical reversal of winds, the stratified baseline experiments are extended until day 225, so that the eddy-field becomes well-developed. At day 225, the passive tracer is reset to its initial state, as shown in the top panel of Figure 3.2. After that, the model is left running for a given period length, before the tracer is reset again, and a new period starts. This is done for prograde and retrograde flow, in addition to an experiment with a wind event. The wind event experiment has a mean prograde flow, but between the 5th and 15th day after the tracer is reset, a wind reversal, as shown in the gray shaded area in Figure 3.4, is present in the forcing. Since we reset the tracer multiple times, several wind reversals are included in the forcing. Depending on the experiment, the period length and the total running time varies. The difference in run-time is simply due to time and resource

limitations. An overview of the experiments are shown in Table 3.5.

Table 3.5: Characteristics of numerical experiments intended for investigating the effect of eddy-activity and periodical reversal of winds on the cross-slope tracer transport. The period length signifies how long the model is run between each reset of the tracer field.

Experiment	**Flow direction**	**Canyon**	**Start day**	**End day**	**Period length**
EXT-R-C	Retrograde	Yes	225	325	10
EXT-R-NC	Retrograde	No	225	325	10
EXT-P-C	Prograde	Yes	225	425	10
EXT-P-NC	Prograde	No	225	425	10
EXT-W-C	Prograde	Yes	225	425	25
EXT-W-NC	Prograde	No	225	425	25

CHAPTER 4

Results

In this chapter, we will go through the results from the numerical experiments described in Section 3.5. First, we will consider the general flow patter over a canyon, as seen in the baseline experiments. Then, we will compare model runs with the theoretical model described in Chapter 2. Finally, we examine the cross-slope tracer transport, both in the initial flow stages, and at later stages when the eddy field has developed. Here, we will also look at the effect of wind reversal on predominantly prograde flow. In all the following results, the daily mean model output values are used in the calculations.

4.1 General flow pattern

We will start by looking at the general flow pattern that evolves in the baseline experiments described in Table 3.2 containing a canyon. Figure 4.1 shows the streamlines for the mean flow at 95 m depth in the vicinity of the canyon between day 40 and 50. The shelf is situated at 100 m depth, so the flow 5 m over the shelf break is shown. Similar streamlines are found for other periods and depths as well (not shown).

In the two leftmost panels in Figure 4.1, the flow in a system without stratification is shown. Panel a. shows the response to wind from the north, setting up a retrograde flow. In panel b., the winds are from the south, establishing a prograde flow. Upstream of the canyon, both the retrograde and prograde flow exhibits the same pattern, with streamlines running parallel to the shore in the same direction as the wind.

At and downstream of the canyon, however, the flow pattern differs considerably between the two flow directions. In the prograde case, the flow veers onshore for the first half of the canyon, and then steers back to its earlier cross-shore position. In the process, the flow crosses isobaths, so that the streamlines resemble a smoothened version of the bathymetry. Downstream of the canyon, the streamlines are again parallel to the shore, resulting in streamlines symmetric about the canyon axis. In contrast, there is a strong signal downstream of the canyon in the retrograde case. The flow turns onshore in the canyon, and a wave-like pattern is formed downstream, with the flow crossing isobaths back and forth. From the width of the streamlines, which indicate flow speed, we can see that the flow downstream of the canyon has the highest velocity.

The two rightmost panels in Figure 4.1 show streamlines for retrograde (panel c.) and prograde (panel d.) flow in a stratified system. These experiments have similar features as the experiments without stratification, with the prograde flow being symmetric about the canyon axis and the retrograde flow exhibiting a wave-like pattern downstream of the canyon. However, the streamlines at 95 m depth are to a lesser degree altered by the canyon in the stratified experiments, compared to the experiments without stratification. In the prograde case, the onshore detour of the flow is smaller than in the corresponding case without stratification. In the retrograde situation, the signal originating at the canyon ceases closer to the canyon in the stratified case. Additionally, the distance between troughs and crests of the disturbance is longer in the stratified case.

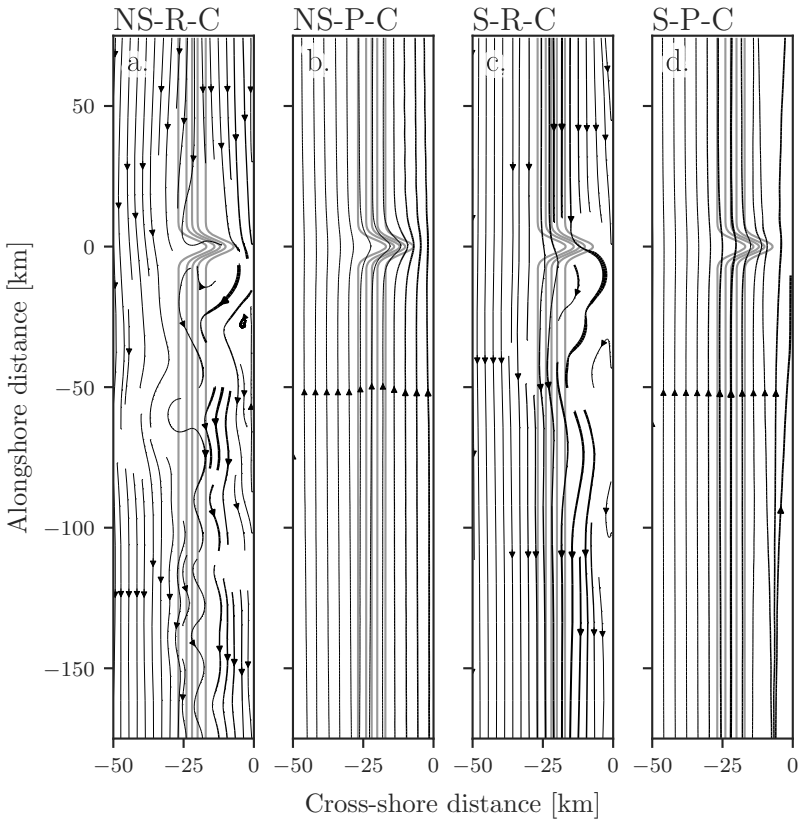

Figure 4.1: Streamlines depicting the mean flow at 95 m depth between model day 40 and 50. Panel a. and b. show the flow pattern in a system without stratification, while panel c. and d. show a stratified system. Panel a. and c. show the response to retrograde flow, while panel b. and d. show the response to prograde flow. Width of the streamlines indicate flow speed, with wider streamlines implying stronger flow. The 150, 225, 300, 375, and 450 m isobaths are shown in gray.

In order to survey the time evolution of the flow, Hovmöller diagrams of the sea surface height (SSH) anomaly at the middle of the slope at x=−22 km are

shown in Figure 4.2 and Figure 4.3. These diagrams are based on the baseline experiments in Table 3.2.

In Figure 4.2, Hovmöller diagrams for experiments without stratification are shown. The two top panels, a. and b., show model runs with retrograde flow, while the two bottom panels, c. and d., show runs with prograde flow. To the left, in panel a. and c., the responses to a topography without any canyon are shown, while panel b. and d. show the responses when a canyon is included.

From panel a. and c., it is clear that there is negligible meridional variation in SSH over the slope in the absence of a canyon. This is a sign of the flow being stable. In the experiments where a canyon is included, similar behavior as in the plot of the mean streamlines in Figure 4.1 can be found. Specifically, the response is symmetric around the canyon axis and confined to the proximity of the canyon in the prograde case, while disturbances can be seen downstream of the canyon in the retrograde case. Looking at panel b., one can see that in the retrograde case, the disturbances form a wave pattern with alternating positive and negative anomalies, gradually extending downstream over time. Eventually, the wave response wraps around the whole domain, reaching the canyon from the upstream side.

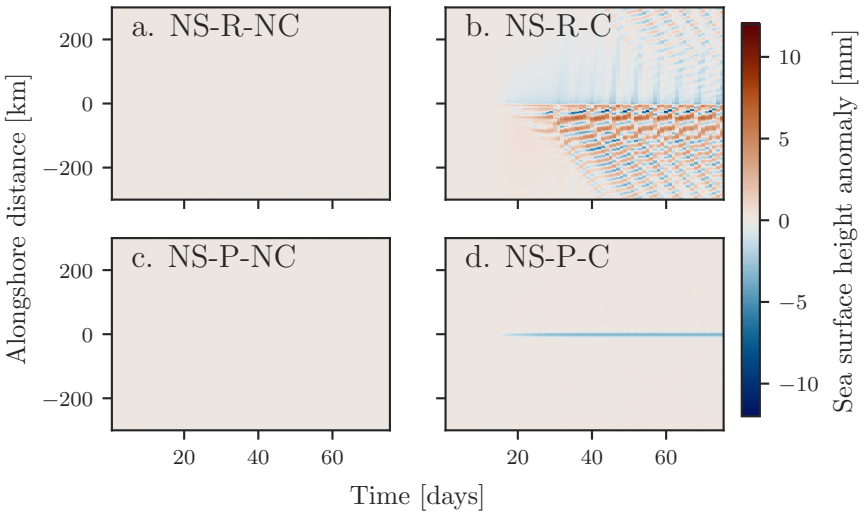

Figure 4.2: Hovmöller diagrams of SSH anomalies at the middle of the slope (x=−22 km) for the first 75 model days in a system without stratification. Panel a. and b. show the response to retrograde flow, while panel c. and d. show the response to prograde flow. In panel a. and c., the bathymetry does not include a canyon, while panel b. and d. contain a canyon. Red and blue show positive and negative anomalies, respectively.

Figure 4.3 shows similar Hovmöller diagrams as Figure 4.2, but for experiments with stratification. In this case, meridional anomalies in the SSH can be seen also in the experiments without a canyon, chiefly after day 50. This is a sign of the formation of eddies, developing due to baroclinic instability. Comparing the inclination of the SSH anomalies to the integrated mean meridional surface

velocity, shown as a gray line, the anomalies seem to propagate slower than the mean surface current. This is in accordance with theoretical models of baroclinic instability, like the Eady model, which predicts the propagation speed of the perturbations to be equal to the mean flow speed at the midpoint in the vertical (Vallis, 2017, pp. 365–366). Because of the vertical shear in the velocity, this speed is smaller than the surface speed.

Comparing panel b. in Figure 4.3 with the corresponding panel in Figure 4.2, we can see that the wave-like features in the stratified system is less pronounced, but still present, especially close to the canyon and at later time-steps. As for the system without stratification, the signal originating at the canyon extends downstream over time, and eventually reaches the canyon again at the upstream side.

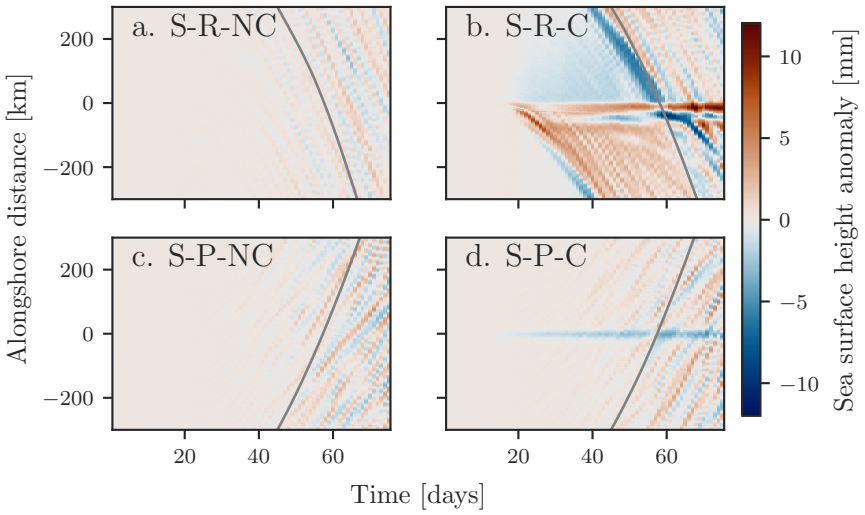

Figure 4.3: Hovmöller diagrams of SSH anomalies for the first 75 model days in a stratified system. Panel a. and b. show the response to retrograde flow, while panel c. and d. show the response to prograde flow. In panel a. and c., the bathymetry does not include a canyon, while panel b. and d. contain a canyon. Red and blue show positive and negative anomalies, respectively. The gray line is the integrated mean meridional surface velocity, integrated from day 45 and shifted to start at $y = \pm 300$.

Until now, we have considered the early flow stages, before the eddy field has developed to any considerable degree. But, as stated in our research questions, we are interested in how eddy activity affects the flow, and specifically the cross-slope transport. We therefore want to estimate when the eddy field becomes well-developed. To do so, we compute the time evolution of the EKE. For each time step, this is calculated as

$$\mathrm{EKE} = \frac{1}{V} \sum_i \frac{1}{2} \left(u_i'^2 + v_i'^2 \right) V_i, \tag{4.1}$$

where $u_i' = u_i - \overline{u}_i$ and $v_i' = v_i - \overline{v}_i$ are deviations from the mean velocities in grid box i. Mean velocities $\overline{u}_i$ and $\overline{v}_i$ are calculated as the temporal moving

average, with a window size of 20 days. This window size is chosen so that transient eddies wouldn't project onto the mean to any considerable degree. V is the total volume of the domain, while V_i is the volume of grid box i.

We also calculate the mean kinetick energy (MKE), which is the kinetic energy associated with the mean flow. MKE is given by

$$\mathrm{MKE} = \frac{1}{V} \sum_i \frac{1}{2} \left(\overline{u}^2 + \overline{v}^2 \right) V_i. \tag{4.2}$$

Figure 4.4 shows the evolution of MKE (top) and EKE (bottom) up to day 315 for stratified systems. These are similar runs as the stratified baseline experiments, but for an extended period. Both retrograde and prograde flow are shown, with and without a canyon.

We can see that in all cases, the EKE increases until about day 150. After day 150, prograde systems with and without a canyon seem to stabilize, fluctuating around a value of about $1.2 \times 10^{-3}\,\mathrm{m}^2/\mathrm{s}^2$. For the retrograde experiments, the case without a canyon seems to stabilize around a value of $2 \times 10^{-3}\,\mathrm{m}^2/\mathrm{s}^2$ after day 175, while the case containing a canyon keeps increasing for the whole period.

The MKE, on the other hand, increases much earlier than the EKE. When the increase in EKE accelerates, the MKE decreases slightly, suggesting that some of the energy in the mean flow is transferred to the eddy field. At around day 175, the retrograde runs stabilize around a value of about $9 \times 10^{-3}\,\mathrm{m}^2/\mathrm{s}^2$, while the prograde runs stabilize around a lower value of about $7 \times 10^{-3}\,\mathrm{m}^2/\mathrm{s}^2$ around day 150.

To illustrate how the intensity of the vorticity increases, snap-shots of the relative vorticity field for stratified retrograde flow over a canyon at different stages are shown in Figure 4.5. Here, contour plots of the daily mean of the depth-averaged relative vorticity for model day 25, 75, 150, 225 and 300 are shown.

As we can see from the leftmost panel in Figure 4.5, an area with higher, contrasting vorticity develops downstream of the canyon already at day 25. As time passes, the vorticity increases, especially at the shelf and slope area. At day 225, we see that eddy-features have developed over the deeper ocean. These seem to continue to develop, as we see more eddy activity over the deep ocean at day 300.

4.2 Comparison with quasi-geostrophic theory

Before we proceed into flow stages with high eddy activity, and investigate how this affects the cross-slope exchange, we will dwell a bit on earlier flow stages where the canyon response is not yet superimposed with a strong vorticity field. Specifically, we will evaluate the theoretical model derived in Chapter 2.

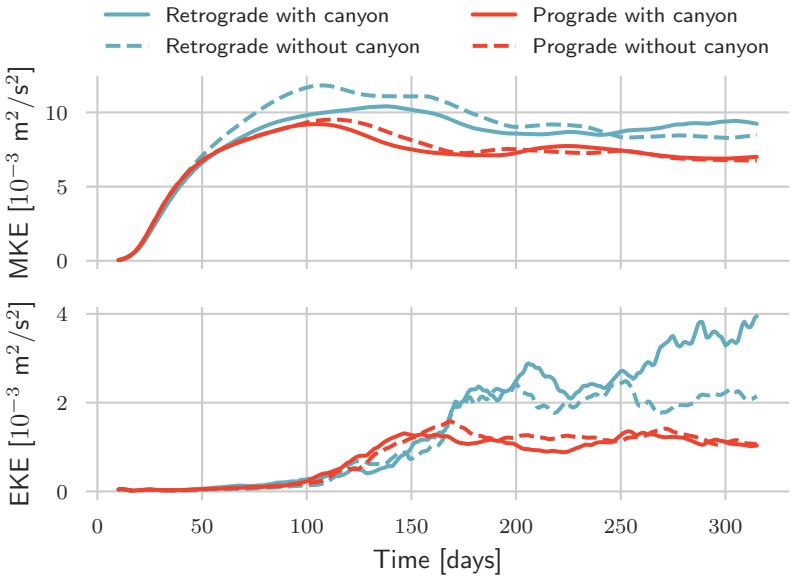

Figure 4.4: Time evolution of MKE (top) and EKE (bottom) in a stratified system up to model day 315. Both MKE and EKE are normalized with the total volume. Blue and red lines represent retrograde and prograde flow, respectively. Model runs including a canyon are shown as solid lines, while dashed lines represent model runs without a canyon.

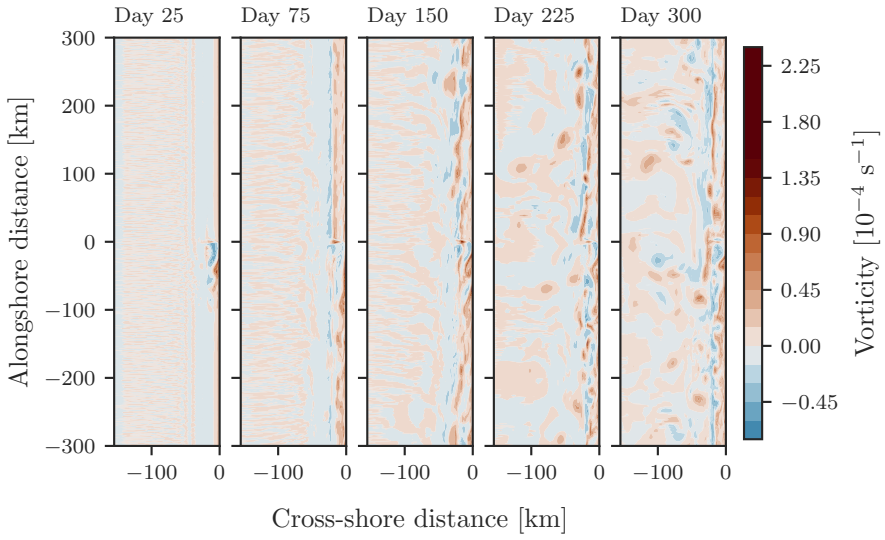

Figure 4.5: Evolution of the depth-averaged relative vorticity field for stratified retrograde flow over a canyon. The mean values for day 25, 75, 150, 225 and 300 are shown.

Prograde flow

We will qualitatively evaluate the applicability of the theoretical model for prograde flow by studying the flow pattern over the canyon, both in a stratified and unstratified system.

As earlier noted, streamlines coincide with the streamfunction contours. We therefore inspect the streamlines that form over the canyon, to see if these are in accordance with the theoretical model, as elaborated in Section 2.5.

In Figure 4.6, streamlines for prograde flow over a canyon in a system without stratification are shown for selected time steps, where the velocity is still increasing. Above each panel, the day and estimated wavenumber of the corresponding arrested wave for the area is included. Since we are considering prograde flow, this wavenumber is calculated as $|\kappa^2_{s,bt}|^{\frac{1}{2}}$, where $\kappa^2_{s,bt}$ is given by Equation (2.9). For simplicity, we will address this value as the arrested wavenumber in this section, even though there are no arrested waves in our prograde runs. As for evaluating Equation (2.9), the variables are taken as the mean values for the plotted area. In addition, the arrested wavenumber is normalized with the value corresponding to the top-left panel.

Further, the correlation between one of the streamlines (shaded red) and the isobath starting at the same southern boundary point as the streamline is included, together with the mean absolute x-distance between said streamline and isobath. A smaller mean absolute distance and higher correlation coefficient corresponds to the streamlines following the bathymetry to a larger degree. By comparing the different panels and associated values, we can get an idea of how the response evolves in time and changes dependent on the arrested wavenumber.

In all cases, the flow detours onshore and resembles a smoothened version of the isobaths, with the most pronounced onshore detour at the middle of the slope. For the first days, we also see that the flow makes a slight offshore adjustment, indicating an initial adjustment to the wind forcing. This affects both the correlation and absolute distance parameter, since the streamline veer slightly offshore. However, we do see a trend of declining correlation and increasing mean absolute distance between the streamline and isobath as the arrested wavenumber decreases.

Figure 4.7 is the equivalent to Figure 4.6, but for a stratified system. Note that when computing $\kappa^2_{s,bc}$, the vertical shear was not taken into consideration, and both V_b and V_0 was approximated by the mean meridional velocity for the given area. However, as we are only interested in the time evolution of the arrested wavenumber, these approximations are deemed reasonable. Also note that different time steps are selected than in the unstratified case, which was done because the flow take longer to stabilize in the stratified system.

A similar pattern can be found as in the system without stratification, with close to symmetric streamlines around the canyon axis and the flow making an onshore detour at the canyon. Additionally, there is a general tendency of increasing mean absolute distance between the streamline and isobath with time. The correlation, however, is fairly constant, except for a decrease in the third to last and last time step. Overall, we see that the arrested wavenumber

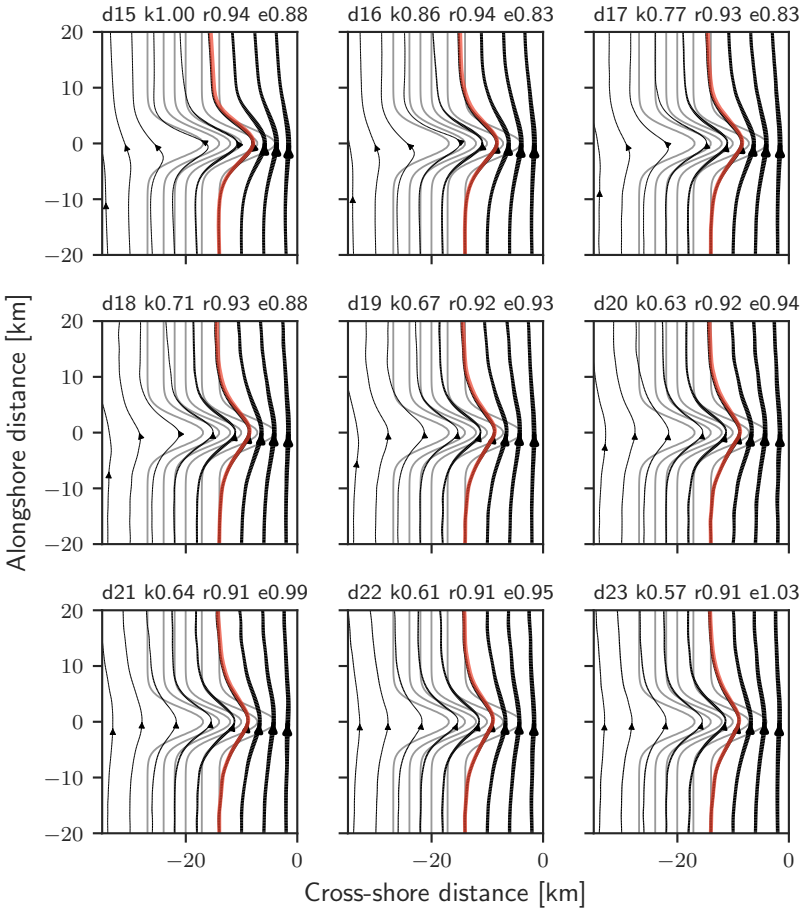

Figure 4.6: Streamlines depicting the response to prograde flow over a canyon in a system without stratification at 95 m depth at selected time steps. The corresponding day (d), normalized arrested wavenumber for the depicted area (k), Pearson correlation coefficient between the streamline marked in red and an isobath (r) and the mean absolute x-distance between said streamline and isobath (e, with units km) are written over each panel. Width of the streamlines indicate flow speed, with wider streamlines implying stronger flow. The 150, 225, 300, 375, and 450 m isobaths are shown in gray.

decreases with time, simultaneously as the flow seems to make a smaller onshore detour, resulting in straighter streamlines.

As discussed in Section 2.4, quasi-geostrophic theory predicts that both stratified and unstratified flow will act as a longpass filer of the topography, with less and less weight on shorter wavelengths as the arrested wavenumber decreases. This can be seen from the amplitude spectrum of the prograde streamfunction response, shown in Figure 2.1. In this figure, the wavenumbers are normalized with the arrested wavenumber; as the arrested wavenumber decreases, less weight is put on larger wavenumbers in the response, again resulting in smoother flow. So the behavior we see in Figure 4.6 and Figure 4.7 is indeed in qualitatively accordance with our theoretical model, signifying that GQ theory can qualitatively describe the prograde flow response over a canyon.

Retrograde flow

In the retrograde case, validation of the theoretical model can be done by comparing the measured and theoretical wavelength of the arrested wave in model experiments. To ensure a variation of wavelengths, multiple experiments, as described in Table 3.3 and Table 3.4, are taken into consideration.

In order to estimate the wavelength λ_m of the arrested wave in model runs, the SSH along the middle of the slope at x=-22 km downstream of the canyon at a given time step is inspected. Especially in model runs with no stratification, there is a clear wave signal in the SSH. In stratified experiments, the signal is generally more noisy, with variations in noisiness between time steps. Therefore, the unstratified experiments are all evaluated at the same time step (day 75), while the stratified experiments are evaluated at varying time steps, specified in Table 3.4. When the wave signal is located visually, autocorrelation is used to estimate the wave length.

Here, autocorrelation is calculated as the Pearson correlation between the SSH data and its shifted self. The along-shore distance that corresponds to the shift giving the first maximum autocorrelation value is then interpreted as the wavelength of the signal.

The theoretical wavelength λ_t of the arrested waves is calculated for the same time step as λ_m. Given the expression for the arrested wavenumbers in Equation (2.9) and Equation (2.21), the wavelength can be computed as $\lambda = 2\pi/\kappa$. This wavelength is dependent on bathymetry, flow characteristics and, in the baroclinic case, the stratification. These variables vary both vertically through the water column and horizontally across and along the slope. To handle this, the meridional mean of relevant variables are calculated first. The vertical variation is handled by computing the mean value for the water column. In the baroclinic case, where vertical variations in the velocity is relevant, the depth dependent velocity is approximated by the linear function minimizing the squared error. Then, for each x-position over the slope, the theoretical wavelength for that position is calculated. Finally, the mean of these wavelengths is calculated.

To evaluate the degree of agreement between λ_t and λ_m, the root mean square

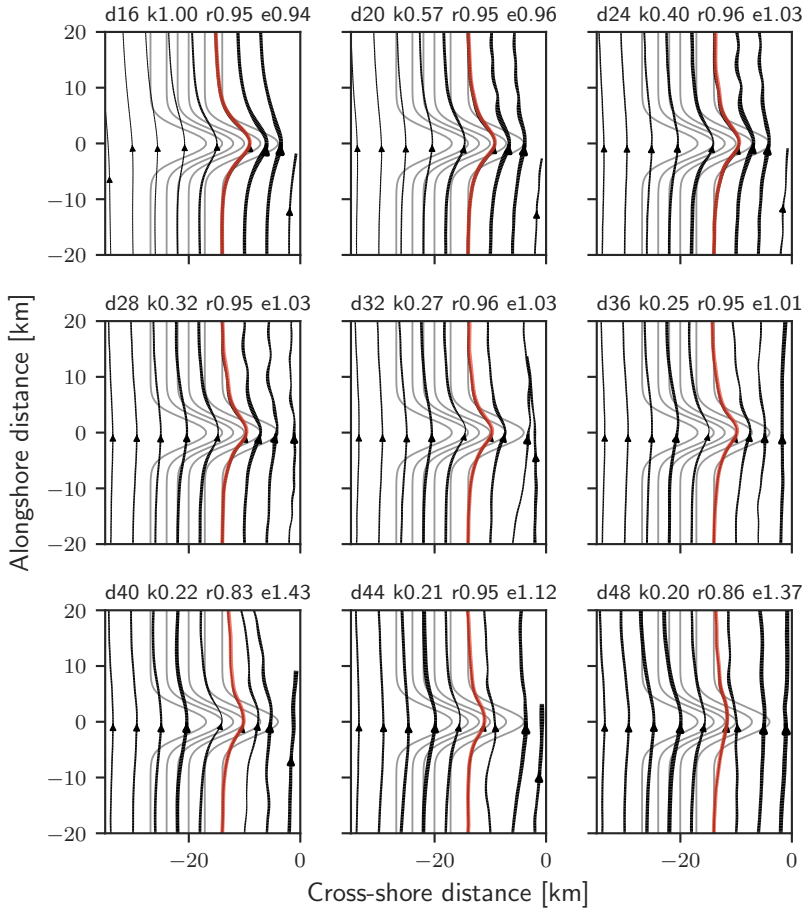

Figure 4.7: Streamlines depicting the response to prograde flow over a canyon in a stratified system at 95 m depth. The corresponding day (d), normalized arrested wavenumber for the depicted area (k), Pearson correlation coefficient between the streamline marked in red and an isobath (r) and the mean absolute x-distance between said streamline and isobath (e, with units km) are written over each panel. Width of the streamlines indicate flow speed, with wider streamlines implying stronger flow. The 150, 225, 300, 375, and 450 m isobaths are shown in gray.

deviation (RMSD) is computed. RMSD can be calculated as

$$\text{RMSD} = \sqrt{\sum_{i=1}^{n} \frac{\left(\lambda_m^i - \lambda_t^i\right)^2}{n}}.$$

where λ_m^i and λ_t^i is the modeled and theoretical wavelength for the ith experiment, and n is the number of experiments.

In Figure 4.8, λ_t is plotted against λ_m for unstratified, retrograde model runs described in Table 3.3. Since all the model runs are without stratification, the barotropic theoretical wavenumber, given by Equation (2.9), is used to calculate λ_t. From the plot, we can see that both λ_t and λ_m are in the range 35 km to 55 km. The RMSD is 4.6 km, with the experiments labeled $0.5 \times \alpha$ and 4×forcing being marginal outliers. The experiments labeled baseline, 3×forcing and 2×friction has a wider 95% confidence interval for the mean of the theoretical wavelengths, indicating that there is a larger spread in flow characteristics across the slope in these experiments. As we see from the figure, most of the modeled wavelengths are within the confidence intervals for the mean, except for the experiments labeled $0.5 \times \alpha$ and 4×forcing, in which the modeled value lies about 5 km and 1 km outside the confidence interval, respectively. This signifies that there is a good agreement between the quasi-geostrophic theoretical model and numerical model runs. Also, the relatively small RMSD between λ_t and λ_m, compared to the range of λ_t and λ_m, indicates that the calculated mean value λ_t is in good agreement with λ_m.

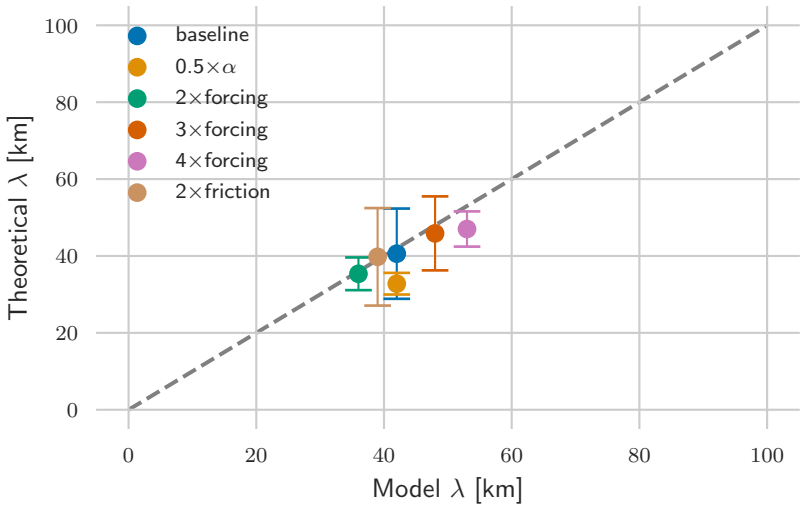

Figure 4.8: Theoretical wavelengths of the arrested barotropic topographic waves as described in Equation (2.9) plotted against the wavelengths found in model runs without stratification. Each dot represents an experiment as described in Table 3.3. The error bars show the 95% confidence interval for the mean, while the gray dashed line is the 1-1 line. RMSD is 4.6 km.

Figure 4.9 shows λ_t against λ_m for the stratified experiments described in Table 3.4. Here, the baroclinic theoretical wavenumber of the arrested wave

(Equation (2.21)) is used when computing λ_t. A wider range of wavelengths are found among the stratified experiments compared to the unstratified experiments, with values ranging between 35 km and 80 km. Similarly, the confidence intervals for the mean are wider in the stratified experiments, reflecting that there is a wider range of background parameters over the slope in these experiments, and consequently a wide range of theoretical arrested wavelengths. Here, λ_t lies outside the confidence interval for three out of eight experiments; baseline, $0.5 \times \alpha$ and 2×forcing. Compared with the barotropic case, the fit of λ_t to λ_m is poorer, with a RMSD of 14.5 km. We also see that λ_t generally underestimates the wavelength, except for the experiment labeled sN, where the wavelength is slightly overestimated. Nevertheless, the theoretical model seems to capture features of the canyon response, as we do see a linear dependency in Figure 4.9.

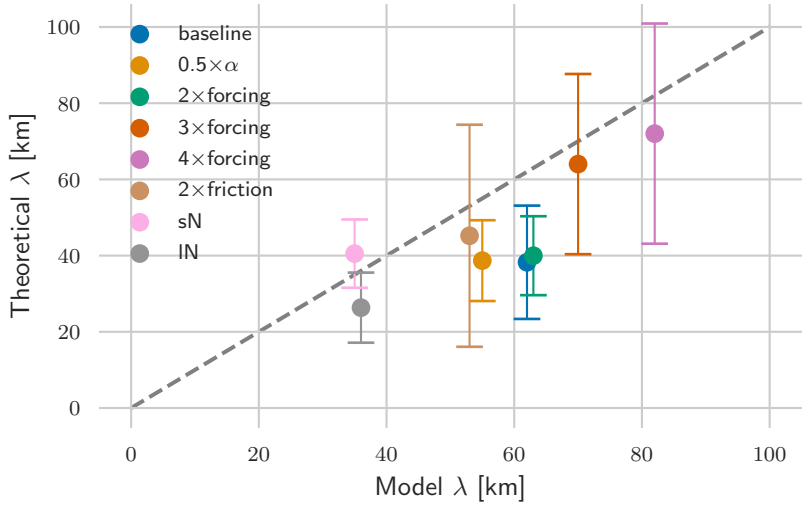

Figure 4.9: Theoretical wavelengths of the arrested baroclinic topographic waves as described in Equation (2.21) plotted against the wavelengths found in model runs with stratification. Each dot represents an experiment as described in Table 3.4. The error bars show the 95% confidence interval for the mean, while the gray dashed line is the 1-1 line. RMSD is 14.5 km.

For corresponding experiments in the stratified and unstratified experiments, we see that λ_m, and to a degree also λ_t, are larger in the stratified experiments. We have seen signs of this earlier as well, as in Figure 4.1, where the distance between peaks in the streamlines are larger in the stratified retrograde case compared with the unstratified retrograde case.

Despite a large scatter and a systematic tendency of underestimating the wavelength in the stratified case, there is surprisingly good agreement between the theoretical model and model simulations in both the stratified, and especially the unstratified systems. Considering the many simplifications and assumptions in the quasi-geostrophic theoretical model, the tendency of a linear dependency we see between λ_t and λ_m is not given. Notably, the assumption that variations in the bottom height is small compared to the mean depth is not realized, as

the change in depth between the shelf and the deep ocean is of the same order as the mean depth.

4.3 Cross-slope tracer transport

In this section, we will consider the cross-slope water exchange, estimated by cross-slope tracer transport. As described in Section 3.3, the tracer is initialized so that the concentration is 1 over the deep ocean, and 0 over the shelf. Over the slope, the tracer concentration has the same shape as the bathymetry. So by computing the net cross-slope tracer transport, we get a measure of how much deep ocean water is transported onto the shelf and stays there. We expect the tracer to be transported by possibly three mechanisms: 1) Ekman transport, 2) eddy transport and 3) canyon effects. These mechanisms are not necessarily isolated from each other, as the canyon could affect the eddy field, for example.

In the case of Ekman transport, the wind stress sets up either an onshore or offshore Ekman flow in the upper layer, depending on the wind direction. This leads to either upwelling or downwelling at the shelf, and sets up a counter-flow lower in the water column. Depending on the wind direction, either the upper or lower flow will transport deep ocean water onto the shelf, while the opposite flow will transport shelf water with a lower tracer concentration into the deeper ocean.

As we saw from the time series in Figure 4.4, the EKE increases with time, before it stabilizes around some value. An exception seems to be the retrograde canyon run, where the EKE doesn't stabilize during our run time. For the first 75 days, the EKE is considerably smaller compared to later staged, indicating little eddy activity. At later time steps, the effect of the eddy field can no longer be ignored. We will therefore look at the tracer transport both in the early stage until day 75, and in later stages, after day 225, and thus be able to examine the transport with and without a well-developed eddy field.

In order to compute net cross-slope passive tracer transport, the zonal tracer transport is integrated over a vertical plane situated at the middle of the slope at x$=-22$ km. The vertical plane extends along the whole slope, so that the net mean mass transport through the plane over time is zero. The total transport is then normalized with the area of the plane, so that the unit of the tracer flux is mass per unit area per time.

Setting up a passive tracer to estimate cross-slope exchange is beneficial over studying the volume transport, since we are able to estimate the property transport across the slope. However, as time passes and tracer is transported onto the shelf, the cross-slope tracer gradient is reduced. As a result, the net onshore tracer transport is reduced, even if the actual water exchange remains constant. As a consequence of this, differences in tracer transport between an experiment with high transport and an experiment with less transport can decrease over time, since the tracer gradient in the experiment with higher transport is reduced faster.

Early stages

The cumulative, i.e., time integrated, tracer transports across the slope for the first 75 days are shown in Figure 4.10. Since the area in which the net flux is calculated over covers the whole yz-plane, and there are no sinks or sources of tracer, this value can be interpreted as the mass of tracer accumulated on the shelf for the given day. The top panel shows the cumulative tracer transport in the unstratified baseline experiments, while the bottom panel shows the results from the stratified baseline experiments. In each panel, experiments with retrograde and prograde flow, and with and without a canyon, are shown. In all cases, the transport in the first 10 model days is zero, agreeing with the model being at rest for this period. For the following days, the cumulative tracer transport increases almost linearly, showing that there is a build-up of tracer at the shelf.

Comparing corresponding model runs with and without a canyon, we see a difference for the experiments with retrograde flow, with a larger transport in the canyon runs. Especially in the unstratified cases is there a substantial difference. In the prograde experiments, the difference between canyon and no-canyon runs is minimal, indicating that the canyon has little effect on the total transport under prograde flow conditions. Still, these model runs exhibit substantial cross-slope tracer transport, meaning that other processes than those connected to a submarine canyon, e.g., Ekman and eddy transport, also yield ample cross-slope exchange.

To better demonstrate the difference between canyon and no-canyon runs and isolate the canyon effect, the difference in cumulative tracer transport between canyon runs and no-canyon runs is shown in Figure 4.11. For all experiments, the difference is minimal in the first 20 days, which includes the 10 days when the model is at rest. In the top panel, which is depicting the experiments without stratification, there is a steady increase in the difference in cumulative tracer transport after day 20 in the retrograde experiment. This translates to the canyon run showing a consistent larger transport than the no-canyon run for retrograde flow direction. There is also an increase in the difference for the stratified retrograde experiments until about day 45. Between the 45th and 60th day, the difference decreases. After day 60, the difference increases a bit and then stays constant. It should be noted that at this time, we have starting eddy-formation, in addition to pronounced reduction in the cross-slope tracer gradient, which most likely affect the tracer transport. For the prograde model runs, the difference between canyon and no-canyon runs is negligible.

In Figure 4.12, the cumulative tracer transport up to day 50 is shown as a function of alongshore position. The baseline experiments containing a canyon is shown, with the left and right panels showing unstratified and stratified systems, respectively. In both prograde situations, we see onshore transport in the canyon upstream of the canyon axis, and then a seemingly equally large offshore transport downstream of said axis. However, the magnitude of the transport is 3-4 times as large in the unstratified case. This pattern can be connected to the onshore detour we have seen in the prograde flow streamlines, as this would result in volume transport onshore upstream of the canyon axis, and then offshore volume transport downstream of the axis. The difference in magnitude can be contributed to the larger detour in the stratified system.

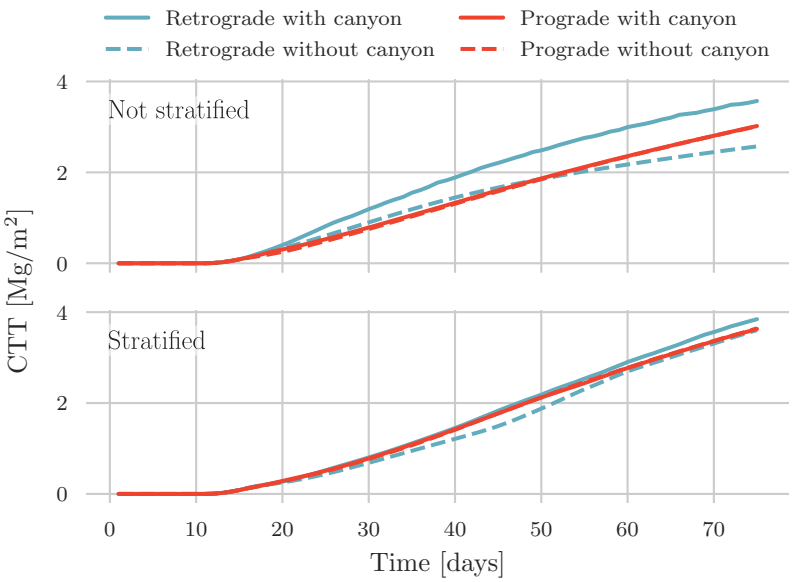

Figure 4.10: Cumulative tracer transport (CTT) across the slope at x=-22 for the first 75 model days for retrograde and prograde flow, both with and without a canyon. Top panel shows the transport for a system without stratification, while the bottom panel shows the transport in a stratified system. Blue and red lines represent retrograde and prograde flow, respectively. Model runs including a canyon are shown as solid lines, while dashed lines represent model runs without a canyon.

For the retrograde flow in an unstratified system, there is a wave pattern of alternating onshore and offshore cumulative transport downstream of the canyon, with decreasing magnitude further from the canyon. A qualitatively similar pattern is found in the stratified case, but here the wavelength of the signal is larger, and the magnitude is smaller and decreases faster. Again, this is the same tendency as we saw in the mean streamlines in Figure 4.1 and in the values for λ_m in Figure 4.8 and Figure 4.9.

Later stages

We will now concentrate on the transport in later flow stages, where the eddy field is more developed. In all the following results, only stratified systems are considered. As stated in our research question, we are interested in whether high eddy-activity affect the cross slope exchange due to a submarine canyon. Especially, we are interested in 1) whether we still see an effect of the canyon in retrograde cases, even in a turbulent field, and 2) if the canyon affects the transport in prograde flow when eddies are present, in contrast to early flow stages.

First, we want to get an idea whether the flow responds similarly to a canyon in a highly turbulent field, as in earlier stages. Figure 4.13 shows streamlines for

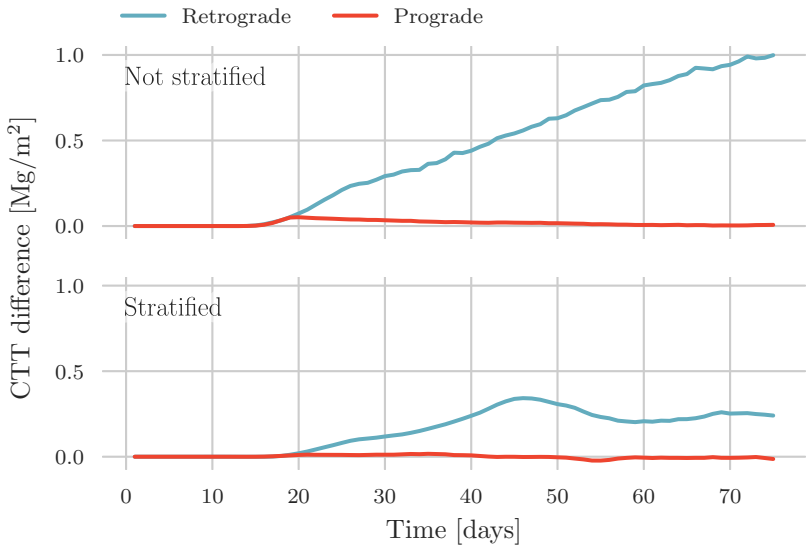

Figure 4.11: Difference in cumulative cross-slope tracer transport between the model runs with and without a canyon in Figure 4.10. Top panel shows the difference in transport for a system without stratification, while the bottom panel shows the difference in transport in a stratified system. Blue and red lines represent retrograde and prograde flow, respectively. Note that both panels have the same scale.

the mean flow at 95 m depth between day 225 and day 325. Taking the mean over a long period, we remove the transient eddy signal from the field. As we see from the left panel, which shows the retrograde response, we still get a lee wave forming downstream of the canyon. In the prograde case, shown in the right panel, we see that the flow acts as a longpass filter of the topography, with a symmetric response around the canyon axis. So, even with a well-developed eddy field, we get a canyon response which is in qualitatively agreement with flow patterns in early stages, and also with our quasi-geostrophic theoretical model.

We will now look at the tracer transport and cumulative tracer transport for retrograde flow in a turbulent field. After day 225, the model is run for a further 100 days, resetting the tracer distribution every 10th day to avoid the tracer becoming fully mixed, and thus no longer acting as a proxy for deep ocean water. Each time the tracer is reset, a new period starts, resulting in a total of 10 periods. All the periods are then superimposed, and the mean is calculated.

Figure 4.14 shows the mean of the tracer transport and cumulative tracer transport for retrograde runs, both with and without a canyon. The values between the 0.1 and 0.9 quantile are shown by the shaded areas. As we can see from the plot of the cumulative tracer transport, model runs with a canyon have more tracer transported to the shelf area than the no-canyon runs, on average. From the top panel, depicting the tracer transport, we see that the difference between canyon runs and no-canyon runs is largest at the beginning of the

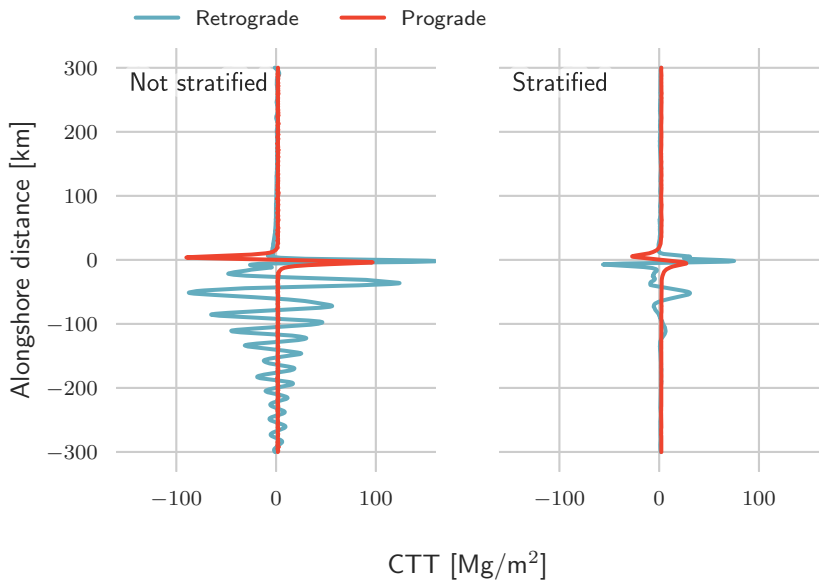

Figure 4.12: Cumulative cross-slope tracer transport up to day 50 as a function of along-shore position in systems containing a canyon. To the left is the cumulative transport in a system without stratification, while the right shows the cumulative transport in a stratified system. Blue and red lines represent retrograde and prograde flow, respectively.

period, when the tracer gradient between the open ocean and shelf is at its largest. To summarize, the increased transport in canyon runs, compared with no-canyon runs, indicates that a canyon still enhance the cross-slope transport in retrograde flow, even under turbulent conditions.

Figure 4.15 is constructed similarly as Figure 4.15, but for prograde flow. Additionally, the model is run until day 425, resulting in a total of 20 periods. As we see from the top panel, the second day has the largest transport, with transport decreasing as time passes after that. This difference between prograde and retrograde in which day shows the largest transport runs is probably due to opposite directions of the Ekman overturning in the two cases, combined with the domain geometry.

Here, in the prograde case, there is no substantial difference between canyon and no-canyon runs in tracer transport. Admittedly, there is a slightly higher transport in the canyon runs for the first day, but this difference is quickly evened out.

Wind event

Our final research question was whether periodical reversal of winds could affect the cross-slope exchange under mean prograde flow over a canyon. To investigate this, a composite plot is made for prograde flow containing a wind reversal. For more realistic conditions, the wind reversal is implemented in a

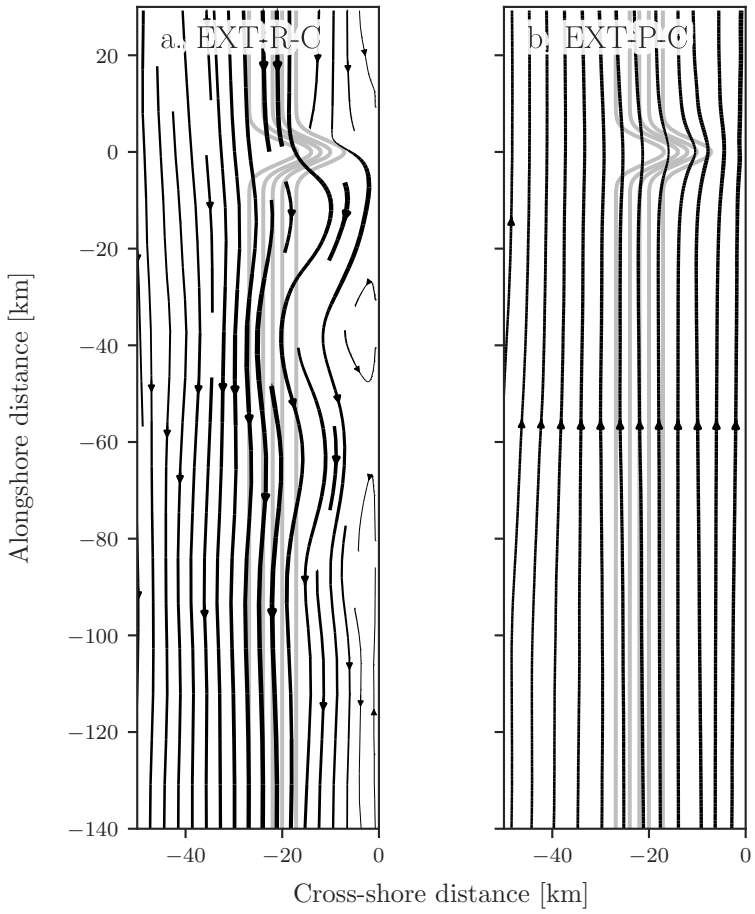

Figure 4.13: Streamlines depicting the mean flow at 95 m depth between model day 225 and 325. Panel a. shows prograde, stratified flow over a canyon, while panel b. shows retrograde, stratified flow over a canyon. Width of the streamlines indicate flow speed, with wider streamlines implying stronger flow. The 150, 225, 300, 375, and 450 m isobaths are shown in gray.

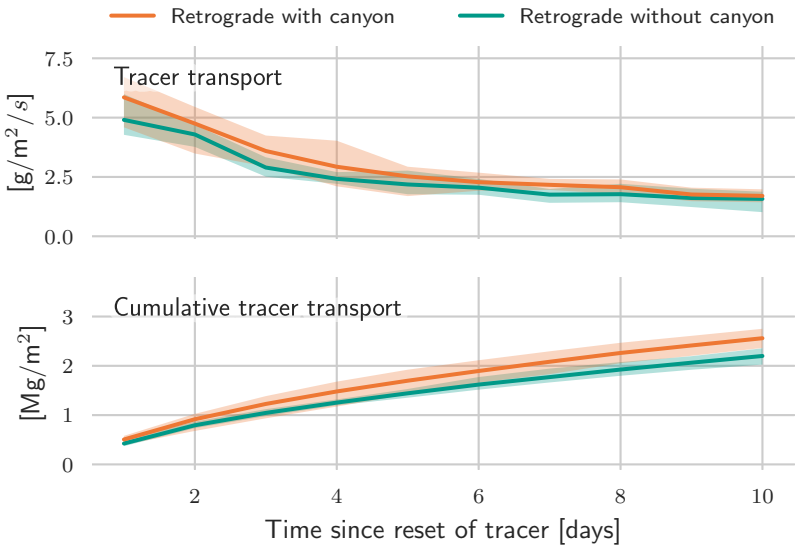

Figure 4.14: Composite plot of cross-slope tracer transport and cumulative tracer transport in turbulent, stratified systems for retrograde flow. Orange and teal represents systems with and without a canyon, respectively. Only model runs after model day 225 are included. The model ran until day 325, and the tracer was reset every 10 days. Each time the tracer is reset, a new period starts, resulting in a total of 10 periods. The solid line is the mean of all the periods, while the shaded area shows the values within the 0.1 to 0.9 quantile.

model state with high eddy activity. The model is run from day 225 until day 425, where the tracer is reset every 25 days, resulting in a total of 8 periods. In each period, a wind event starts at the fifth day, and lasts for 10 days. The wind stress evolution during the wind event has the form of one sinusoidal cycle, with actual reversal of winds for a total of 5 days, as illustrated in Figure 3.4. For consistency between the periods, the first period is discarded, as this period is not preceded by a wind event.

The resulting mean tracer transport and cumulative tracer transport is shown in Figure 4.16. From the bottom panel, we see that there is a larger mean cumulative tracer transport in the canyon runs, compared to no-canyon runs. Surprisingly, the difference in transport between canyon runs and no-canyon runs is largest outside the wind event, while the mean tracer transport is about equal for the two cases during the wind event. As each period follows after another period containing a wind event, the difference in transport that we see right after the concentration reset must be caused by the previous wind event.

In order to assess whether the wind event results in reversal of bottom flow direction, and thus opens for the possibility of arrested topographic waves as an explanation for the increased transport, the mean meridional bottom velocity for the same periods as in Figure 4.16 is shown in the top panel in Figure 4.17. We see that the velocity decreases from wind event day 2 (period day 7), and starts to increase again at wind event day 8 (period day 13). In other words,

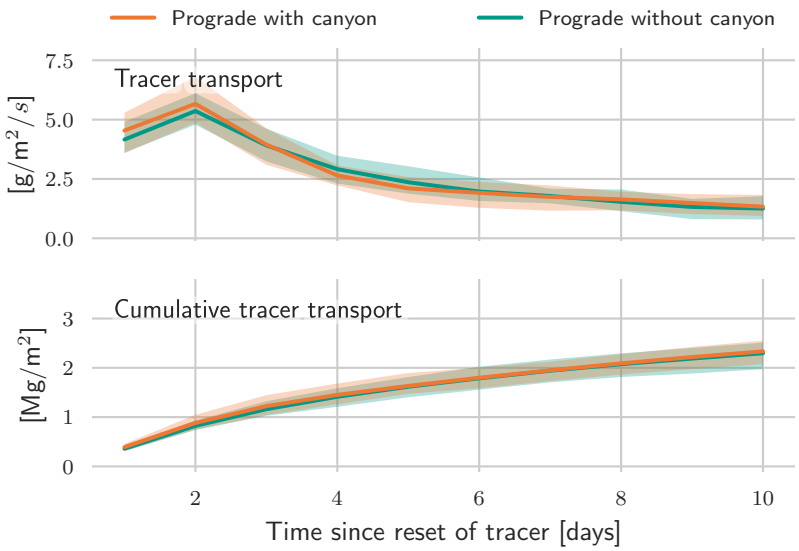

Figure 4.15: Composite plot of cross-slope tracer transport and cumulative tracer transport in turbulent, stratified systems for prograde flow. Orange and teal represents systems with and without a canyon, respectively. Only model runs after model day 225 are included. The model ran until day 425, and the tracer was reset every 10 days. Each time the tracer is reset, a new period starts, resulting in a total of 20 periods. The solid line is the mean of all the periods, while the same colored shaded area shows the values within the 0.1 to 0.9 quantile.

the bottom velocity roughly reflects the change in wind forcing, shifted with about 2 days. We can also see that the meridional bottom velocity is generally slightly stronger in the cases without a canyon. This is not the case in mode runs without wind reversal (not shown). Note that even though the velocity decreases, the direction does not change. So, one possible condition for having arrested topographic waves is not present.

Another possibility for achieving arrested waves is through strong vertical shear in the flow, so that the term containing $\partial_z V$ in Equation (2.19) becomes strongly negative. Then, the condition in Equation (2.19) for an arrested wave can still be satisfied, even though V_b is positive. But inspection of the velocity data shows that this is not the case. In other words, the increase we see in tracer transport in wind event runs can not be explained with our theoretical model for arrested topographic waves.

In Figure 4.17, the bottom panel shows the mean EKE for the wind event periods. Here, EKE is computed slightly differently than in Equation (4.1). Since the forcing, and consequently the mean flow, is not constant, interpreting the perturbations u_i' and v_i' as deviations from the temporal mean flow could yield faulty results. Instead, we assume $u_i' = u_i - \widetilde{u}_i$ and $v_i' = v_i - \widetilde{v}_i$, where $\widetilde{u}_i$ and $\widetilde{v}_i$ are meridional mean values.

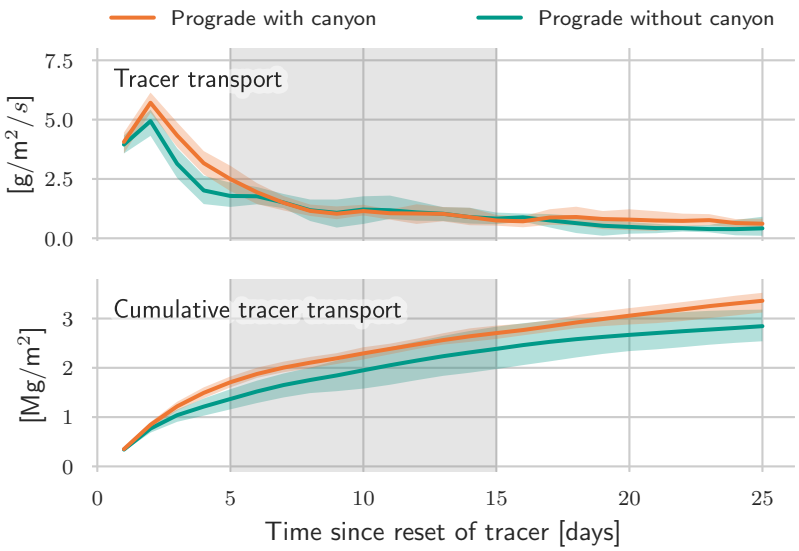

Figure 4.16: Composite plot of cross-slope tracer transport in turbulent, stratified systems for initially prograde flow with a wind event. Orange and teal represents systems with and without a canyon, respectively. Only model runs after model day 250 are included. The model ran until day 425, and the tracer was reset every 25 days. Each time the tracer is reset, a new period starts, resulting in a total of seven periods. Each period has one wind event, shown as the gray shaded area. The solid line is the mean of all the periods, while the same colored shaded area shows the values within the 0.1 to 0.9 quantile.

As we see from Figure 4.17, the EKE is higher in the no-canyon runs, especially before day 7, and after around day 17. Again, since the composite plot is cyclic, the increase at the beginning of the period is most likely due to the previous wind event. Comparing the top panels in Figure 4.16 and Figure 4.17, we see that the period with increased EKE in no-canyon runs coincides with the period where we also have higher tracer transport in canyon runs. One could think that the heightened transport in canyon runs could be due to more eddies in these runs, but surprisingly Figure 4.17 shows the opposite. As for now, the detailed dynamics behind the heightened transport in canyon runs with periods of reversed winds are not fully understood.

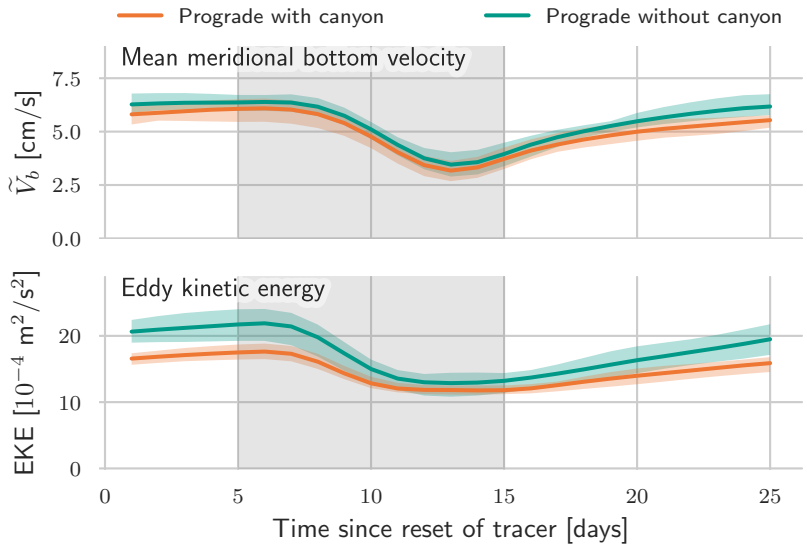

Figure 4.17: Composite plot of mean meridional bottom velocities along the slope (top) and mean EKE (bottom) in turbulent, stratified systems for initially prograde flow with a wind reversal. EKE is calculated from perturbations from the meridional mean values, and not from the temporal mean values. Orange and teal represents systems with and without a canyon, respectively. The plots are composed of seven periods, as in Figure 4.16. Each period has one wind event, shown as the gray shaded area. The solid line is the mean of all the periods, while the same colored shaded area shows the values within the 0.1 to 0.9 quantile.

CHAPTER 5

Discussion

5.1 Quasi-geostropic theory and canyon flow

From our comparison between numerical model simulations of flow over a canyon, and the corresponding quasi-geostrophic theoretical models, we found good agreement, especially for unstratified systems, indicating that the simplified quasi-geostrophic models does indeed describe important qualitative and quantitative aspects of the dynamics.

During the development of the theoretical model, we found that it was important to include the horizontal potential vorticity gradient stemming from the x-shear in the meridional flow. In our approach, we assumed the velocity to have a constant vertical shear, but the theoretical model opens for other approximations for the flow, which can be tailored to the specific application. It should be noted that not all forms for the velocity give analytical solutions. One possibility that does, is an exponential structure in the vertical for the velocity.

The mechanism of arrested topographic waves interacting with the topography, and thus causing an asymmetrical response to flow in opposite directions along the slope, has already been investigated by Zhang and Lentz, 2017. By the use of a model for coastal trapped waves, as described in Brink, 1990; Brink, 2006, Zhang and Lentz were able to calculate the wavelength of the downstream meander forming in retrograde simulations. However, contrary to the model presented in this thesis, their model has to be solved numerically. The model presented here is thus easier to implement, and less resource-demanding. Additionally, one of the advantages of an analytical model describing the flow response is the intuitive understanding it provides us. From our analytical expressions, we can see how changes in geometry, hydrographic properties and flow characteristics influence the response.

Especially, we see that the amplitude of the streamfunction response depends both on the spectrum of the topography, and the amplitude spectrum plotted in Figure 2.1, which is given by flow characteristics, stratification, latitude, mean depth and steepness of the slope. The lesser overlap there is between the amplitude spectrum of the topography and the amplitude spectrum of the streamfunction response to a white spectrum, the less pronounced will the response be. Likely, this will lead to a smaller cross-slope exchange. As a practical application, an estimate of the response to a given bathymetry can thus be calculated for varying flow and hydrographic conditions as given by

Equation (2.11) and Equation (2.22), without the need of refined numerical methods. Similarly, given the stratification and flow, one can estimate the canyon dimensions needed for a considerable response. We can then make rough prior estimates of which canyons that should give a larger response.

It should also be noted that Saldías and Allen, 2020 preformed the same numerical analysis as Zhang and Lentz, 2017 for retrograde alongshore flow over a canyon, without finding a connection between the characteristics of the flow response, and the coastal trapped wave. The numerical set-up of Saldías and Allen, 2020 is similar to that used in this thesis, but their model is only run for 25 days, which means that the analysis of Saldías and Allen was preformed in earlier flow stages compared to the analysis in this thesis. This indicates that the wavelength of the lee wave forming downstream of the canyon may be controlled by some other mechanisms as well, at least in initial flow stages. In that case, QG theory may not be as well suited for initial flow stages.

5.2 Possible mechanisms behind on-shelf tracer transport

As expected, based on results from earlier studies of prograde and retrograde flow over canyons, the cross-slope tracer transport in our simulations is enhanced by the canyon in retrograde flow, while the transport in prograde flow regimes is nearly unaffected by the inclusion of a canyon, at least for constant wind forcing. This is true for both the stratified and the unstratified case. As an important result, we found that this is also true for a highly turbulent field.

The wave structure forming downstream of the canyon in retrograde flow regimes results in water being transported back and forth over the slope (see Figure 4.1). This motion in itself does not necessarily result in displacement of deep ocean water to the shelf area, as the net mass flux must be zero over time. However, if there are some irreversible processes present that result in mixing of water properties, like turbulent diffusion, deep ocean properties can be mixed in with the current over the deeper parts of the slope, and then transported onto the shelf and mixed in with the shelf water. This way, the arrested wave can transport shelf water properties to the deep ocean and deep ocean properties back on to the shelf, resulting in net transport of e.g. nutrients onshore. As we see in Figure 4.12, which shows the cumulative tracer transport as a function of alongshore position, the tracer is indeed transported back and forth in a wave-like structure. The difference in the extent of the downstream wave pattern between the unstratified and stratified system in the initial period is also consistent with the bigger difference in tracer transport between canyon and no-canyon runs in the unstratified system than in the stratified system for the same period. The picture is different in the prograde cases, where the mean flow follows the isobaths both upstream and downstream of the canyon. As we have seen, the flow does make an onshore detour over the canyon, given the right combination of flow characteristics and likely also canyon width. One could expect a similar effect as discussed for the retrograde flow, where deep ocean properties are transported onshore and mixed with adjacent water masses on the shelf. But, in the prograde case, this would happen over a much smaller section, making a considerably smaller contribution to the cross-slope transport.

As a result, the transport is almost equal in canyon and no-canyon runs in the prograde initial model runs.

Here, we have focused on how a large horizontal detour of the prograde flow can increase the transport. But, under conditions where the flow makes a smaller detour, the flow crosses more isobaths, consequently resulting in larger vertical velocities along the canyon walls. These vertical velocities can lead to increased vertical mixing in the canyon, possibly increasing the nutrient concentration in the euphotic zone locally in the canyon. Since this process doesn't necessarily result in tracer crossing the slope, this effect is not detected in our analysis.

5.3 Applicability to LoVe

The inspiration for this thesis was the flow over submarine canyons off the LoVe archipelago, and whether the large fish stocks, many whale sightings and otherwise high bioproductivity in this area can be linked to enhanced cross-slope transport of nutrients induced by canyons. As described in the introduction, the Norwegian Atlantic Slope Current follows the shelf break in this area, with the coast to the right, making it a prograde flow.

The question arises whether the behavior predicted by quasi-geostrophy is applicable to the LoVe region. From our theoretical model for the flow response in a stratified model, given in Equation (2.22), we would expect prograde flow to follow the isobaths to a larger degree when the current velocity is lower. For higher velocities, we would expect the current to flow in a more straight manner over the topography, crossing more isobaths. A tendency of this is seen in our idealized model, as shown in Figure 4.7. But what about in more realistic simulations? In Figure 5.1, borrowed from Matuszak, 2021, backwards in time particle trajectories for a realistic model domain based on the LoVe ocean region, computed using OpenDrift simulations, are plotted. These trajectories are illustrative of the paths of particles prior to reaching the Hola reef, which is situated at the bottom of a canyon in LoVe. Both summer (June 2020) and winter (December 2020) conditions are shown, with velocities taken from the Norkyst-800 model. In summer, the current velocity is lower than in winter. Consequently, we can see that the particle trajectories for the summer, as seen in Figure 5.1a, follows the canyon walls closely, without much depth change. In the winter, however, the particles flow almost straight over the canyon wall, as we can see in Figure 5.1b. In other words, there is good qualitatively agreement between the quasi-geostrophic model and idealized numerical simulations presented in this thesis, and more realistic numerical simulations. This further indicates that the results presented here are indeed applicable to LoVe.

As we have seen, a single canyon has little effect on the cross-slope transport under prograde conditions even in a turbulent field, at least for persistent alongshore wind forcing. However, we saw that when we included subsequent periods with reversal of the wind stress, the canyon did in fact enhance the transport, even if the flow did not change direction. But how relevant is this for LoVe? Figure 5.2 shows monthly wind rose plots for Røst airport, which is situated on the outermost island south-west in Lofoten. Assuming that observations from this station are representative for the whole region, the wind

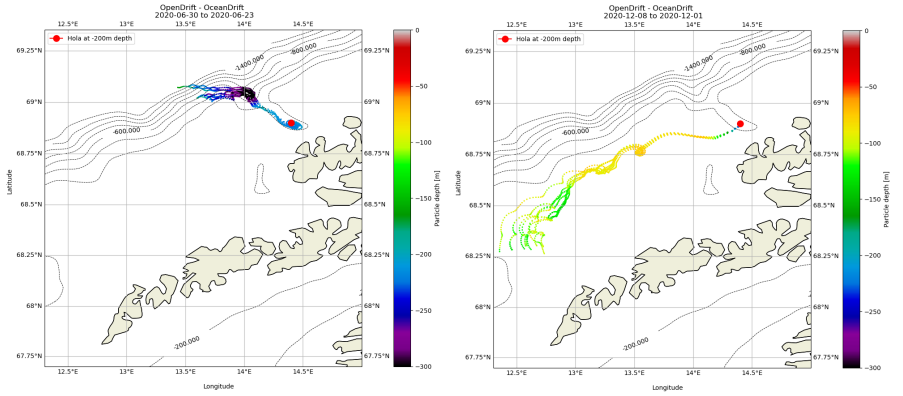

(a) Particle trajectories of ten particles released on 30th of June 2020, tracked backwards in time until 23rd of June 2020.

(b) Particle trajectories of ten particles released on 8th of December 2020, tracked backwards in time until 1st of December 2020.

Figure 5.1: Backwards in time trajectories for ten particles released at the ocean bottom in a 100 m radius around the Hola Reef. The particles are released at 30th of June 2020 and 8th of December 2020, and traced back for a week. Hola is marked in red. Bottom topography is indicated by gray contours, with a 200 m depth interval between each contour line. The particle depth is indicated by their color. Figure courtesy of Matuszak, 2021.

rose plots can give us information on the distribution of wind directions and speeds through the year over the slope. Keeping in mind that the slope is situated along the south-west to north-east axis, we see that the wind does indeed occasionally blow in the opposite direction of the current. Especially in the summer season, in the period April to August, a substantial amount of the measurements show winds coming from the north, signifying that a considerable component of the wind blows in the opposite direction of the current. So the submarine canyons off the North-Norwegian coast could indeed cause enhanced cross-slope exchange even if the flow is prograde, due to reversal of winds.

Another possible reason for enhanced exchange is the effect of multiple subsequent canyons. Looking at the map over the LoVe basin in Figure 1.1, we see that multiple canyons cut into the shelf break, with about 10 km distance between them. As predicted by quasi-geostrophic theory and confirmed in model runs, the current makes an onshore detour over the canyon. One can therefore hypothesize that when the canyon density is high, the prograde flow can exhibit a wavelike structure over the shelf break, transporting water masses back and forth over the slope multiple times, resulting in onshore transport of nutrients through mixing. Or, given flow conditions that the flow passes almost straight over the canyons, the vertical velocities along the canyon walls might cause considerable transport of nutrients. In other words, even though we saw little effect of one canyon, the net effect of multiple canyons may be notable.

5.4 Limitations

Finally, we discuss some limitations of this study.

In this study, the domain had an along-shore length of 600 km, while the canyon itself had a width of about 10 km. When calculating the cross-slope transport, this had to be done along the whole domain length, in order to have conservation of mass. Since cross-slope transport due to Ekman transport and turbulent mixing happens along the whole domain, and the extent of the domain is considerably larger than that of the canyon, the effect of the canyon can be outweighed, especially if the effect is highly localized in the canyon. This is relevant especially in the prograde model runs.

In addition, it should be mentioned that the model simulations presented in this thesis are relatively short, considering that we are investigating the effect of eddies. As shown in the time evolution of EKE in Figure 4.4, the eddy field in the retrograde simulations with a canyon doesn't seem to stabilize in the period we are looking at. For a more robust analysis, longer runs would be necessary.

Finally, the way the theoretical and modeled wavelength of the arrested topographic wave is detected and calculated needs to be addressed. Especially in the stratified model runs, the downstream wave response could be hard to detect, and the analysis had to be preformed for varying time steps between the experiments in order to find a clear signal. Most likely, the unclear signal is due to eddies affecting the SSH. In order to have better estimates of the wavelength of the arrested waves, the effect of eddies could have been (partly) removed by calculating the mean SSH over time. Subsequently, the values used to calculate the theoretical wavelengths could also be taken from time-averaged fields.

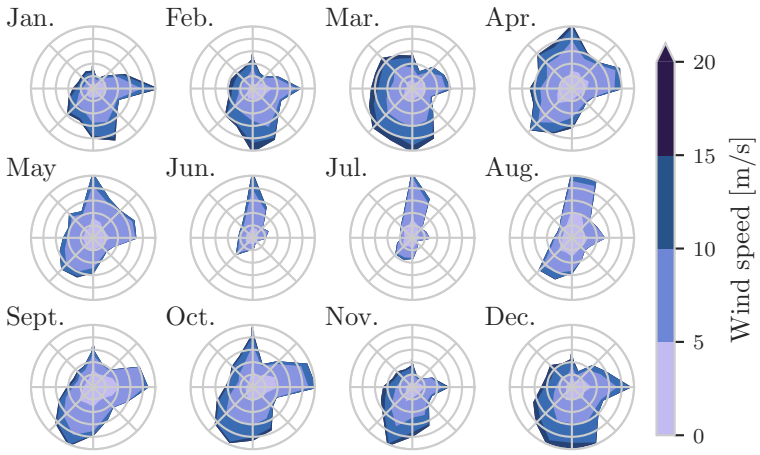

Figure 5.2: Monthly wind rose plots of Røst airport wind observations. The contours show the speed distribution and the direction the wind is coming from, with northerly to the top. Observations are hourly mean values for the period May 1st 2011 to May 1st 2021, fetched from the Norwegian Centre for Climate Services, seklima.met.no.

CHAPTER 6

Conclusion

This final section concludes the thesis, and contains a summary of the study and the main contributions, together with a section on further research.

6.1 Summary and main contributions

An analytical, quasi-geostrophic model for the streamfunction response to flow over a canyon was developed, both for a barotropic and a baroclinic system.

Furthermore, idealized numerical experiments of prograde and retrograde flow along a continental slope, both with and without a canyon, have been set up, run and analyzed. Some of these model runs were compared with the response predicted by the analytical model. Another important aspect was to let the model run long enough to let the eddy field develop, so that the effect of high eddy activity on cross-slope transport difference between canyon and no-canyon runs could be investigated. Additionally, periods of reversed winds was included in some model runs.

There was generally good agreement between the theoretical, quasi-geostrophic model and numerical model runs, indicating that the theoretical model does indeed describe important dynamics in the system. To our knowledge, this is the first analytical model describing flow patterns over a submarine canyon.

As expected, based on results from earlier studies, the canyon enhanced the cross-slope tracer transport under retrograde flow conditions in early flow stages. The difference was largest in stratified experiments. In the prograde case, there were negligible differences between runs with and without a canyon in the initial flow stages. We found that the same was true in a highly turbulent field, with higher transports in retrograde runs with a canyon than in runs without a canyon, and with little effect of the canyon in prograde runs.

However, we found that when periods of reversed winds was present, the canyon did increase the cross-slope tracer transport, even if the mean flow was prograde. The detailed dynamics behind this effect is still unknown.

6.2 Further research

As is the nature of a Master's thesis, the extent of the analysis and numerical experiments is restricted by time limitations. Nevertheless, or maybe because

of that, several ideas for further research have emerged during the writing of this thesis. Here, we present some of these ideas.

When comparing model runs of retrograde flow over a canyon with the theoretical quasi-geostrophic model, we have concentrated on varying parameters affecting the flow characteristics and stratification in order to achieve a spread in the possible wavelengths of the arrested topographic waves. In the prograde case, we focused on different time steps in the flow evolution. In both cases, we kept the canyon geometry constant. However, to further investigate the applicability of quasi-geostrophic theory, we would benefit from systematically varying the canyon geometry, and thus see how the wavenumber spectrum of the topography affects the response when the flow conditions are prescribed. Also, the strength of the response under retrograde flow conditions can be further investigated. For example, one can calculate the Fourier coefficient for the wavenumber of the arrested wave for a given canyon-geometry, and compare this with the strength of the response in numerical simulations. This way, the applicability of quasi-geostrophic theory to flow over a canyon can be further explored.

Additionally, how consecutive canyons affects transport of nutrients onto the shelf, especially in prograde flow regimes, would be of interest to investigate. As we speculated in Section 5.3, this may be relevant for the high bioproductivity in the LoVe ocean region, which has a high concentration of canyons along the continental slope. Since we have worked with a channel domain in this thesis, the effect of the canyon signal propagating downstream and reaching a canyon on the upstream side is present. However, our domain has a meridional length of 600 km, making the distance the signal has to travel before reaching a canyon considerable. So, investigating the effect of a high canyon density could be done either by including several canyons in the model bathymetry, or, alternatively, by shortening the length of the channel.

Finally, further investigation of how periods of reversed winds affects the cross-slope transport of nutrients in LoVe can give us deeper insight regarding mechanisms behind the high bioproductivity in the region. An important finding in this study was that the presence of a submarine canyon enhances the cross-slope transport after periods of reversed winds, even for prograde flow with high eddy activity. The next step could be to conduct realistic model simulations of currents in the LoVe region, where periods of reversed winds are included. This could answer important questions on how canyons can affect the transport of biologically important resources, even under prograde flow conditions.

Appendices

APPENDIX A

Additional figures

Figure A.1 shows the number of observations per depth level, while Figure A.2 shows the geographic distribution of casts used for computations of mean salinity and potential temperature profiles for stratified model runs.

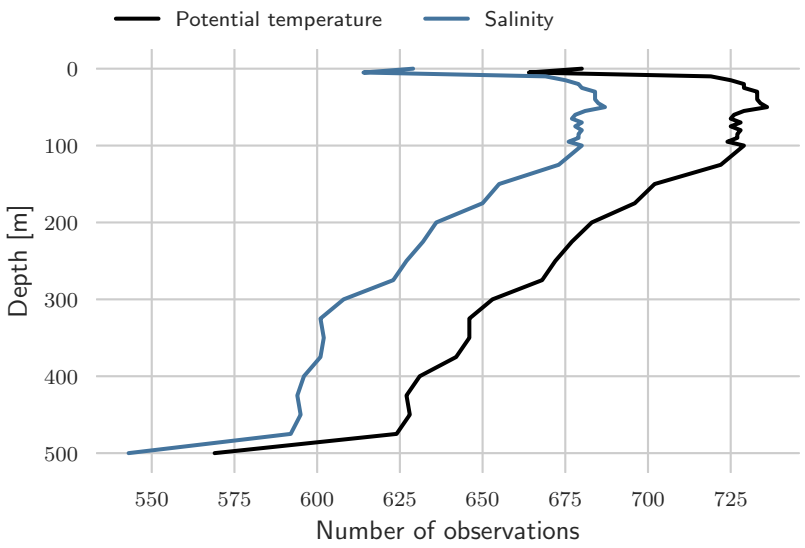

Figure A.1: Number of observations used when calculating mean salinity and potential temperature profiles shown in Figure 3.3.

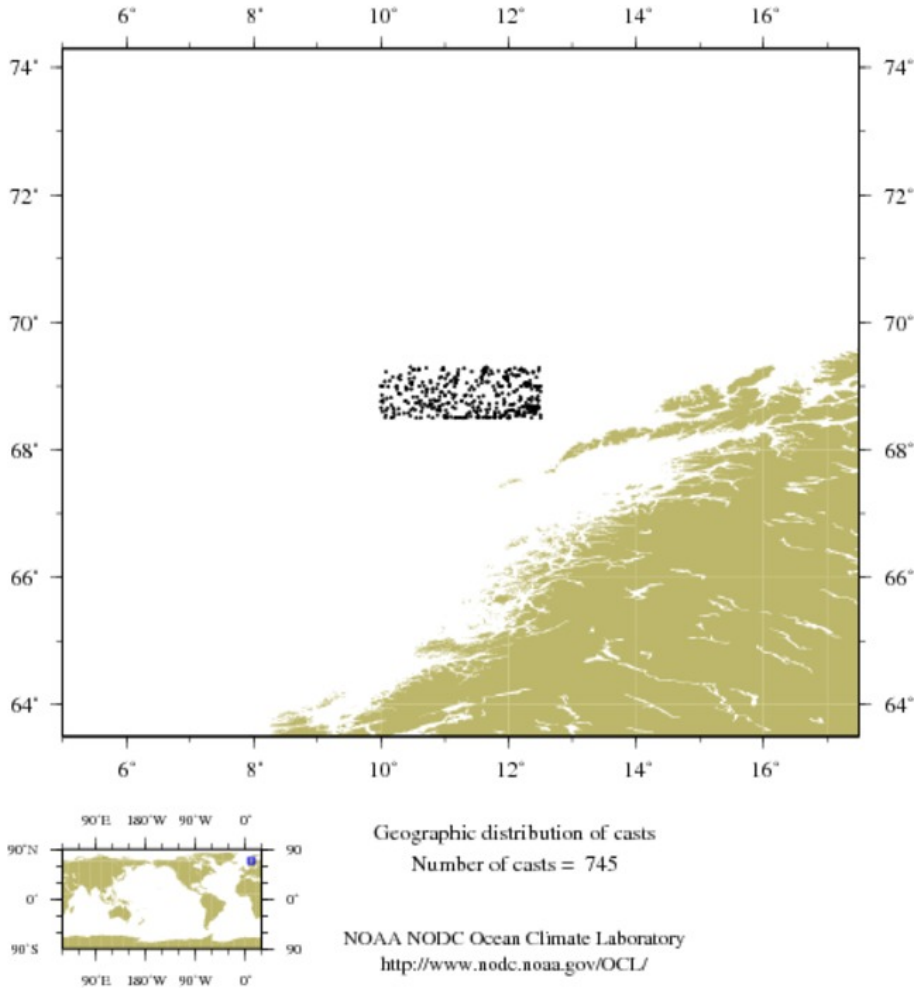

Figure A.2: Geographic distribution of casts providing hydrographic observations used to create Figure 3.3. Casts are restricted to the area 68.5°- 70.0°N, 12.0°- 16.0°E.

APPENDIX B

Derivation of quasi-geostrophic equations

We will here go through a possible way to derive the QGPV equations in order to illuminate which assumptions are made, and how they are applied.

The main assumptions are:

- The flow is in near-geostrophic balance, meaning that the Rossby number $Ro = U/Lf$ is small.
- Variations in the Coriolis parameter are small. Specifically, for a β-plane where the Coriolis parameter can be expressed as $f = f_0 + \beta y$, we have $|\beta L|/|f_0| = \mathcal{O}(Ro)$
- The bottom topography h_B is small compared to the total depth h_0, that is, $|h_B|/h_0 = \mathcal{O}(Ro)$.
- Similarly, the surface elevation η is small compared to the total depth; $|\eta|/h_0 = \mathcal{O}(Ro)$.

To further derive the QGPV equations, we must distinguish between barotropic and baroclinic flow, since the two regimes allow different vertical flow structures.

B.1 Barotropic flow

To arrive at the QGPV equation for barotropic flow, we consider first the shallow water equation for conservation of potential vorticity:

$$\frac{D}{Dt}\left(\frac{f+\zeta}{H}\right) = (\partial_t + \mathbf{u}\cdot\nabla)\left(\frac{f+\zeta}{H}\right) = 0. \tag{B.1}$$

Here, $H = h_0 + \eta - h_B$ is the full layer thickness. The operators ∂_t, ∂_x and ∂_y are partial derivatives with respect to t, x and y, respectively. As is conventional, f is the Coriolis parameter, also referred to as the planetary vorticity, and $\zeta = \partial_x v - \partial_y u$ is the relative vorticity. Equation (B.1) states that the ratio of the absolute vorticity and the fluid depth is conserved following a fluid column. This ratio is what we call the potential vorticity.

Introducing a β-plane, so that $f = f_0 + \beta y$, we see that the shallow water potential vorticity can be written as

$$\begin{aligned}\frac{f+\zeta}{H} &= \frac{f_0 + \beta y + \zeta}{h_0 + \eta - h_B} \\ &= \frac{1}{h_0}\left(\frac{f_0 + \beta y + \zeta}{1 - (h_B - \eta)/h_0}\right) \\ &\approx \frac{1}{h_0}\left(f_0 + \beta y + \zeta\right)\left(1 + \frac{h_B - \eta}{h_0}\right) \\ &\approx \frac{1}{h_0}\left(f_0 + \beta y + \zeta + \frac{f_0(h_B - \eta)}{h_0}\right).\end{aligned} \tag{B.2}$$

The last approximation follows from the quasi-geostrophic assumption that we have a small Rossby number, which is equivalent to f being much larger than ζ. We also have that β is much smaller than f_0, so we only keep the small therm $(h_B - \eta)/h_0$ when multiplied by the relatively large f_0. To make the approximation that

$$\frac{1}{1 - (h_B - \eta)/h_0} \approx 1 + \frac{h_B - \eta}{h_0},$$

we utilize that $h_b - \eta$ is much smaller than h_0, and approximate the fraction as the first two therms in its geometric series.

Substituting Equation (B.2) into Equation (B.1), and noting that the advection of the potential vorticity should be by the geostrophic velocity, we arrive at

$$\frac{D_g}{Dt}\left(\zeta_g + \beta y + \frac{f_0(h_B - \eta)}{h_0}\right) = 0, \tag{B.3}$$

where

$$\frac{D_g}{Dt} = \partial_t + u_g\partial_x + v_g\partial_y.$$

Notice also that we kept only the geostrophic part of the relative vorticity, therefor the subscript.

This is the QGPV equation for barotropic flow, without forcing.

B.2 Baroclinic flow

Here, we will follow an informal derivation of the quasi-geostrophic potential vorticity equation for baroclinic flow, as in Vallis, 2017, p. 193. A more vigorous derivation can be found in the mentioned book.

We start with the vertical component of the vorticity equation, which is obtained by cross-differentiating the horizontal momentum equations. We have

$$\begin{aligned}\frac{D}{Dt}\left(\zeta + f\right) = -\left(\zeta + f\right)\left(\partial_x u + \partial_y v\right) + \left(\partial_z u \partial_y w - \partial_z v \partial_z v \partial_x w\right) \\ + \frac{1}{\rho^2}\left(\partial_x \rho \partial_y p - \partial_y \rho \partial_x p\right).\end{aligned}$$

By the Boussinesq approximation, therms containing the density ρ disappears (except when multiplied with the gravitational constant g), so the last therm is omitted.

We now apply the quasi-geostrophic assumptions. By the first assumption, we replace the velocities on the left hand-side with the geostrophic counterpart. The divergence on the right hand-side is small, but we keep it when it is multiplied with the relatively large Coriolis parameter.

From the second assumption, we have that f can be replaced with the constant f_0, except where it is differentiated.

To show that the second therm on the right hand-side can be omitted, we use a scaling argument. This therm scales as $UW/(HL)$, while the left hand-side scales as U^2/L^2, giving the ratio $[UW/(HL)]/[U^2/L^2] = [W/H]/[U/L]$. This ratio is small, since $\partial_z w \propto W/H$ equals the divergence of the ageostrophic velocity.

We are then left with

$$\frac{D_g}{Dt}\left(\zeta_g + f\right) = -f_0\left(\partial_x u + \partial_y v\right) = f_0 \partial_z w. \tag{B.4}$$

Since the horizontal velocities are geostrophic, they can be replaced with a stream function ψ so that

$$u_g = -\partial_y \psi, \qquad v_g = \partial_x \psi. \tag{B.5}$$

Equation (B.4) then has two unknowns; the stream function ψ and the vertical velocity w. We therefore include a second equation to close the system, namely the thermodynamic equation.

$$\partial_t \rho + \mathbf{u} \cdot \nabla \rho = \frac{D}{Dt}\rho = 0. \tag{B.6}$$

The density ρ is assumed to be nearly constant, so we divide the density into a background density and a perturbation, writing $\rho = \rho_0(z) + \rho'(x, y, z, t)$. We do the same decomposition of the pressure $p = p_0(z) + p'(x, y, z, t)$. We can then write the hydrostatic balance as

$$\partial_z p_0 = -g\rho_0, \qquad \partial_z p' = -g\rho'.$$

Keeping only the geostrophic components of the horizontal velocities, we can write Equation (B.6) as

$$\frac{D_g}{Dt}\partial_z p - wg\partial_z \rho_0 = 0,$$

where we have neglected the vertical advection of the perturbation density, since this is much smaller than the advection of the background density. Hydrostatic and geostrophic balance enables us to define the stream function as a function of the pressure

$$\psi = \frac{p}{f_0 \rho_0},$$

resulting in the equation

$$\frac{D_g}{Dt} f_0 \partial_z \psi + wN^2 = 0. \tag{B.7}$$

Combining Equation (B.4) and Equation (B.7), and thus eliminating w, we get

$$\frac{D_g}{Dt}\left(\nabla^2\psi + \partial_z\left(\frac{f_0^2}{N^2}\partial_z\psi\right) + \beta y\right) = 0. \tag{B.8}$$

This is the QGPV Equation for baroclinic flow.

A lower boundary condition can be found from Equation (B.7). Vertical flow at the lower boundary can come from either flow over topography or Ekman pumping, yielding the lower boundary condition

$$\left.\frac{f_0}{N^2}\frac{D_g}{Dt}\partial_z\psi\right|_{z=z_b} = -\mathbf{u}_g \cdot \nabla h_B - r\nabla^2\psi. \tag{B.9}$$

The first therm on the left hand-side is the vertical flow resulting from flow over topography, while the second therm is the vertical velocity at the top of the Ekman layer, which is proportional to the relative vorticity.

Bibliography

Allen, S. E. and Durrieu de Madron, X. (2009). "A review of the role of submarine canyons in deep-ocean exchange with the shelf." eng. In: *Ocean science discussions* vol. 6, no. 2, pp. 1369–1406.

Ardhuin, F., Pinot, J.-M., and Tintoré, J. (1999). "Numerical study of the circulation in a steep canyon off the Catalan coast (western Mediterranean)." eng. In: *Journal of Geophysical Research: Oceans* vol. 104, no. C5, pp. 11115–11135.

Bosley, K. L., Lavelle, J., Brodeur, R. D., Wakefield, W., Emmett, R. L., Baker, E. T., and Rehmke, K. M. (2004). "Biological and physical processes in and around Astoria submarine Canyon, Oregon, USA." eng. In: *Journal of marine systems* vol. 50, no. 1, pp. 21–37.

Brink, K. (1990). "On the damping of free coastal-trapped waves." eng. In: *Journal of physical oceanography* vol. 20, no. 8, pp. 1219–1225.

— (2006). "Coastal-trapped waves with finite bottom friction." eng. In: *Dynamics of atmospheres and oceans* vol. 41, no. 3, pp. 172–190.

Ciano, J. N. and Huele, R. (2001). "Photo-identification of sperm whales at Bleik canyon; Norway." eng. In: *Marine mammal science* vol. 17, no. 1, pp. 175–180.

Fer, I., Bosse, A., and Dugstad, J. (2020). "Norwegian Atlantic Slope Current along the Lofoten Escarpment." eng. In: *Ocean science* vol. 16, no. 3, pp. 685–701.

Held, I. M. (1983). "Stationary and quasi-stationary eddies in the extratropical troposphere: Theory." In: *Large-scale dynamical processes in the atmosphere* vol. 127, p. 168.

Isachsen, P. E. (2015). "Baroclinic instability and the mesoscale eddy field around the Lofoten Basin: Baroclinic instability in Lofoten basin." eng. In: *Journal of geophysical research. Oceans* vol. 120, no. 4, pp. 2884–2903.

Jordi, A., Klinck, J. M., Basterretxea, G., Orfila, A., and Tintoré, J. (2008). "Estimation of shelf-slope exchanges induced by frontal instability near submarine canyons." eng. In: *Journal of Geophysical Research: Oceans* vol. 113, no. C5, C05016–n/a.

Jordi, A., Orfila, A., Basterretxea, G., and Tintoré, J. (2005). "Shelf-slope exchanges by frontal variability in a steep submarine canyon." eng. In: *Progress in oceanography* vol. 66, no. 2-4, pp. 120–141.

Kämpf, J. and Chapman, P. (2016). *Upwelling systems of the world*. Springer.

Killworth, P. D. (1978). "Coastal Upwelling and Kelvin Waves with Small Longshore Topography." eng. In: *Journal of physical oceanography* vol. 8, no. 2, pp. 188–205.

Klinck, J. M. (1996). "Circulation near submarine canyons: A modeling study." eng. In: *Journal of Geophysical Research: Oceans* vol. 101, no. C1, pp. 1211–1223.

Marchesiello, P., Debreu, L., and Couvelard, X. (2009). "Spurious diapycnal mixing in terrain-following coordinate models: The problem and a solution." In: *Ocean Modelling* vol. 26, no. 3, pp. 156–169.

Matuszak, M. (2021). "Eulerian and Lagrangian description of currents around a coral reef in Lofoten-Vesterålen." BA thesis. University of Oslo.

Moore, A. M., Arango, H. G., Di Lorenzo, E., Cornuelle, B. D., Miller, A. J., and Neilson, D. J. (2004). "A comprehensive ocean prediction and analysis system based on the tangent linear and adjoint of a regional ocean model." eng. In: *Ocean modelling (Oxford)* vol. 7, no. 1, pp. 227–258.

Quillfeldt, C. H. von (2010). *Det faglige grunnlaget for oppdateringen av forvaltningsplanen for Barentshavet og havområdene utenfor Lofoten: Rapport fra Faglig forum, Overvåkingsgruppen og Risikogruppen til den interdepartementale styringsgruppen for forvaltningsplanen.*

Saldías, G. S. and Allen, S. E. (2020). "The Influence of a Submarine Canyon on the Circulation and Cross-Shore Exchanges around an Upwelling Front." eng. In: *Journal of physical oceanography* vol. 50, no. 6, pp. 1677–1698.

Shchepetkin, A. F. and McWilliams, J. C. (2005). "The regional oceanic modeling system (ROMS): a split-explicit, free-surface, topography-following-coordinate oceanic model." eng. In: *Ocean modelling (Oxford)* vol. 9, no. 4, pp. 347–404.

— (2003). "A method for computing horizontal pressure-gradient force in an oceanic model with a nonaligned vertical coordinate." eng. In: *Journal of Geophysical Research - Oceans* vol. 108, no. C3, 3090–n/a.

She, J. and Klinck, J. M. (2000). "Flow near submarine canyons driven by constant winds." eng. In: *Journal of Geophysical Research: Oceans* vol. 105, no. C12, pp. 28671–28694.

Skliris, N. and Djenidi, S. (2006). "Plankton dynamics controlled by hydrodynamic processes near a submarine canyon off NW corsican coast: A numerical modelling study." eng. In: *Continental shelf research* vol. 26, no. 11, pp. 1336–1358.

Skliris, N., Goffart, A., Hecq, J. H., and Djenidi, S. (2001). "Shelf-slope exchanges associated with a steep submarine canyon off Calvi (Corsica, NW Mediterranean Sea): A modeling approach." eng. In: *Journal of Geophysical Research: Oceans* vol. 106, no. C9, pp. 19883–19901.

Søiland, H. and Rossby, T. (2013). "On the structure of the Lofoten Basin Eddy." eng. In: *Journal of geophysical research. Oceans* vol. 118, no. 9, pp. 4201–4212.

Spurgin, J. M. and Allen, S. E. (2014). "Flow dynamics around downwelling submarine canyons." eng. In: *Ocean science* vol. 10, no. 5, pp. 799–819.

Vallis, G. K. (2017). *Atmospheric and Oceanic Fluid Dynamics.* eng. Cambridge: Cambridge University Press.

Zhang, W. and Lentz, S. J. (2017). "Wind-Driven Circulation in a Shelf Valley. Part I: Mechanism of the Asymmetrical Response to Along-Shelf Winds

in Opposite Directions." eng. In: *Journal of physical oceanography* vol. 47, no. 12, pp. 2927–2947.
— (2018). "Wind-driven circulation in a shelf valley. Part II: Dynamics of the along-valley velocity and transport." eng. In: *Journal of physical oceanography* vol. 48, no. 4, pp. 883–904.